**Review Article**

**Open Access**

Florian Wendler, Andreas Knorr, and Ermin Malic*

# Ultrafast carrier dynamics in Landau-quantized graphene

**Abstract:** In an external magnetic field, the energy of massless charge carriers in graphene is quantized into non-equidistant degenerate Landau levels including a zero-energy level. This extraordinary electronic dispersion gives rise to a fundamentally new dynamics of optically excited carriers. Here, we review the state of the art of the relaxation dynamics in Landau-quantized graphene focusing on microscopic insights into possible many-particle relaxation channels. We investigate optical excitation into a non equilibrium distribution followed by ultrafast carrier–carrier and carrier–phonon scattering processes. We reveal that surprisingly the Auger scattering dominates the relaxation dynamics in spite of the non-equidistant Landau quantization in graphene. Furthermore, we demonstrate how technologically relevant carrier multiplication can be achieved and discuss the possibility of optical gain in Landau-quantized graphene. The provided microscopic view on elementary many-particle processes can guide future experimental studies aiming at the design of novel graphene-based optoelectronic devices, such as highly efficient photodetectors, solar cells, and spectrally broad Landau level lasers.

## 1 Motivation

With an ever-growing impact of technology on everyday life, the importance of semiconductor physics has constantly increased since the information revolution. Of particular interest is the field of optoelectronics enabling key technologies for modern communication. The fast techno-logical progress is accompanied by the demand for materials with new optical and electronic properties. One of the most promising materials in this regard is graphene [1–4], which was first grown epitaxially on top of SiC [5], but it was not until Novoselov and Geim prepared samples by mechanical exfoliation and demonstrated a graphene-based field-effect transistor [6] in 2004 that it received wide-spread attention.

Graphene as a single layer of carbon atoms is the thinnest known two-dimensional material [3, 7]. It exhibits extraordinary optical, electronic, thermal, mechanical, and chemical properties [3]. In particular, its linear electronic dispersion in the low-energy regime near the Dirac points in the Brillouin zone is most remarkable. Here, electrons move as if they were massless, just like photons in quantum electrodynamics providing the possibility to test the predictions of relativistic quantum mechanics, such as Klein tunneling [8, 9], in a small-scale table top experiment.

Besides the fascinating fundamental physics that can be explored in graphene, several optoelectronic applications were proposed [1], ranging from ultrafast photodetectors [10–12] and lasers [13–15], to solar cells [16, 17], light-emitting devices [18], and touch screens [19]. However, the question whether graphene can cope with the high expectations and make the way from the laboratory to real world applications remains to be answered. To exploit the full potential of this promising material, a thorough microscopic understanding of the ultrafast dynamics of optically excited charge carriers is crucial. This has been an area of active research for many years [20–37], and has revealed that carrier–carrier and carrier–phonon scattering lead to interesting graphene-specific ultrafast phenomena [38, 39]. In particular, the linear bandstructure of graphene enables Auger scattering [40], an elastic Coulomb process changing the number of charge carriers in the system, that gives rise to a significant carrier multiplication [41–44]. This process holds the potential to increase the power conversion efficiency of solar cells and facilitate the detection of photons [45]. Furthermore, in the strong excitation regime a population inversion emerges as a result of the relaxation bottleneck [31, 34, 46–48] sug-

**\*Corresponding Author: Ermin Malic:** Department of Applied Physics, Chalmers University of Technology, Gothenburg, Sweden, E-mail: ermin.malic@chalmers.se
**Florian Wendler:** Department of Applied Physics, Chalmers University of Technology, Gothenburg, Sweden, E-mail: florian.wendler@tu-berlin.de
**Andreas Knorr:** Institute of Theoretical Physics, Nonlinear Optics and Quantum Electronics, Technical University Berlin, Germany

gesting the use of graphene as an active gain medium in a laser system [49].

An external magnetic field provides an interesting experimental knob to tune electronic and optical properties of graphene including the dynamics of non-equilibrium carriers. In the presence of a magnetic field, the energy is quantized into a non-equidistant Landau level spectrum [50–54] giving rise to an anomalous quantum Hall effect [55, 56]. Moreover, a non-zero Berry's phase, which arises due to the linear dispersion, manifests itself in magneto-oscillations [56]. The observation of a number of interesting phenomena, such as the fractional quantum Hall effect [57, 58], the Hofstadter butterfly [59–61], a giant Faraday rotation [62], the quantum ratchet effect [63], and the presentation of a tunable terahertz detector [64] have attracted considerable research interest to Landau-quantized graphene [65]. However, due to technological challenges and unlike in the case without a magnetic field, the carrier dynamics is widely unexplored under Landau quantization where only a few studies exist [66–69].

In this review, we present microscopic modeling of the carrier dynamics in Landau-quantized graphene based on the density matrix approach, which allows the investigation of many-particle-induced scattering channels on a microscopic footing. First, we describe the microscopic approach including the many-particle Hamilton operator, the coupling matrix elements, and the microscopic Bloch equations (Section II). Then, we present results based on this approach including the impact of carrier–carrier and carrier–phonon scattering (Section III). We show that surprisingly Coulomb-induced Auger scattering dominates the relaxation dynamics in Landau-quantized graphene. In a joint experiment-theory study involving polarization-dependent pump-probe measurements, we present the evidence for the crucial role of these scattering channels [70]. Furthermore, we show that carrier–phonon scattering becomes very efficient, if the energy of the involved optical phonons is in resonance with an inter-Landau level transition presenting the possibility to control this scattering channel by changing the external magnetic field [71, 72]. Finally, we present potential graphene-based applications based on the gained knowledge of the many-particle scattering processes (Section IV). We show that efficient Auger scattering can be exploited to achieve a significant carrier multiplication in Landau-quantized graphene [73]. Through this mechanism, the number of excited charge carriers increases much stronger than expected from optical excitation suggesting the design of novel ultrafast photodetectors or photovoltaic devices. Furthermore, we discuss the possibility to achieve a population inversion in Landau-quantized graphene presenting the prerequisite

for Landau level lasers that are characterized by a strongly tunable laser frequency including the technologically relevant terahertz frequencies [74].

# 2 Microscopic approach

## 2.1 Implementation of the magnetic field

The Lagrange function of an electron in a magnetic field [75]

$$L_B = \frac{1}{2}m_0\mathbf{v}^2 - e_0\mathbf{v} \cdot \mathbf{A}(\mathbf{r}) \tag{1}$$

depends on the gauge invariant kinetic velocity $\mathbf{v}$, and on the vector potential $\mathbf{A}(\mathbf{r})$ which generates the magnetic field via $\mathbf{B} = \nabla \times \mathbf{A}(\mathbf{r})$. In order to obtain a homogeneous magnetic field, which shall point into the z-direction $\mathbf{B} = (0, 0, B)$, the spatial dependence of $\mathbf{A}(\mathbf{r})$ is crucial. The vector potential $\mathbf{A}(\mathbf{r})$ is not unambiguously determined but depends on the chosen gauge. The Landau gauge $\mathbf{A}(\mathbf{r}) = (0, Bx, 0)$ is advantageous for calculations as it transforms the Hamiltonian into the form of a one-dimensional harmonic oscillator, while the symmetric gauge $\mathbf{A}(\mathbf{r}) = B/2 \cdot (-y, x, 0)$ yields a Hamiltonian that can be identified as that of a two-dimensional harmonic oscillator [75]. The latter is mathematically more complex but describes the underlying physics in a more intuitive way, since one expects electrons in a strong magnetic field to perform cyclotron orbits which are oscillations in two dimensions. Furthermore, the symmetric gauge allows a convenient description in terms of angular momentum eigenfunctions.

The canonical momentum $\mathbf{p} = -i\hbar\nabla_{\mathbf{r}}$ is derived from the Lagrange function from Eq. (1) with $\mathbf{p} = \nabla_{\mathbf{v}}L_B$ providing a simple substitution rule: To accommodate for the magnetic field, one needs to replace the momentum $\mathbf{p}$ by the kinetic momentum $\boldsymbol{\pi} = m_0\mathbf{v}$

$$\mathbf{p} \to \boldsymbol{\pi}(\mathbf{r}) = \mathbf{p} + e_0\mathbf{A}(\mathbf{r}), \tag{2}$$

which yields the Hamiltonian via a Legendre transformation $H_B = \boldsymbol{\pi}^2/(2m_0)$. Note that the spatial dependence of the Hamiltonian $H_B$ destroys the translation invariance, with the result that neither the kinetic nor the canonical momentum commutes with $H_B$ meaning they are no longer conserved quantities.

For electrons in a rigid ionic lattice, such as graphene, the situation is more complicated, since the potential of the positively charged atom cores $V(\mathbf{r})$, obeying the periodicity $V(\mathbf{r} + \mathbf{R}) = V(\mathbf{r})$, additively contributes to the Hamiltonian. In the absence of a magnetic field, the full Hamiltonian is symmetric under the translation by lattice vectors

**R**, which is exploited to find the wave function of a particle in a periodic lattice potential. This is a simple Bloch wave $\Psi(\mathbf{r}) = e^{i\mathbf{k}\cdot\mathbf{R}}u(\mathbf{r})$ consisting of a phase $e^{i\mathbf{k}\cdot\mathbf{R}}$ and a periodic function with the same periodicity of the lattice $u(\mathbf{r} + \mathbf{R}) = u(\mathbf{r})$ [76]. In a magnetic field, the missing translation invariance of $H_B$ impedes the use of the Bloch solution [77], which is only valid, if the translation operator $T_{\mathbf{R}} = e^{i\mathbf{k}\cdot\mathbf{R}}$ commutes with the full Hamiltonian. Instead, a new momentum operator commuting with $H_B(\boldsymbol{\pi})$ is defined [78]

$$\tilde{\boldsymbol{\pi}}(\mathbf{r}) = \mathbf{p} - e_0\mathbf{A}(\mathbf{r}), \tag{3}$$

allowing the construction of a magnetic translation operator $T_{B,\mathbf{R}} = e^{i\tilde{\boldsymbol{\pi}}(\mathbf{r})\cdot\mathbf{R}/\hbar}$ [79, 80]. While the so called pseudo-momentum $\tilde{\boldsymbol{\pi}}$ commutes with the kinetic momentum $\boldsymbol{\pi}$, its components do not commute $[\tilde{\pi}_x, \tilde{\pi}_y] = ie_0\hbar B_z$, and one finds

$$T_{B,\mathbf{R}}T_{B,\mathbf{R}'} = \exp\left(-i2\pi\frac{\mathbf{B}\cdot\mathbf{R}\times\mathbf{R}'}{\phi_0}\right)T_{B,\mathbf{R}'}T_{B,\mathbf{R}}, \tag{4}$$

with the magnetic flux quantum $\phi_0 = h/e_0$. Therefore, the group of magnetic translation operators is non-abelian, with the consequence that the motion in a magnetic field induces an Aharanov–Bohm phase [81]. However, if $\mathbf{B}\cdot\mathbf{R}\times\mathbf{R}'$ yields a rational multiple of $\phi_0$, the periodicities of the crystal lattice and cyclotron orbits are commensurable, an abelian subgroup $T_{B,\mathbf{R}_s}$ of $T_{B,\mathbf{R}}$ exists, and a magnetic superlattice may be obtained by searching for superlattice vectors $\mathbf{R}_s$, for which the exponential in Eq. (4) is always one [82], i.e. $T_{B,\mathbf{R}_s}T_{B,\mathbf{R}'_s} = T_{B,\mathbf{R}'_s}T_{B,\mathbf{R}_s}$. Then, the periodicity of the superlattice allows to establish a generalized Bloch theorem similar to $\Psi(\mathbf{r}) = e^{i\mathbf{k}\cdot\mathbf{R}}u(\mathbf{r})$, where $\mathbf{R}$ is replaced by $\mathbf{R}_s$, and $\mathbf{k}$ is restricted to a magnetic Brillouin zone. The construction of the magnetic superlattice is such that each unit cell of the superlattice intercepts precisely one magnetic flux quantum [83].

Note that while the Aharanov–Bohm phase results from the spatial dependence of the vector potential $\mathbf{A}(\mathbf{r})$ destroying the translation invariance of the Hamiltonian, the existence of a magnetic superlattice can be regarded to reflect the homogeneity of the magnetic field which implies that the orbit of an electron in a magnetic field (cyclotron orbit) is independent of its position. In fact, both concepts can be brought in line through a singular gauge transformation of the wave function transforming the vector potential $\mathbf{A}(\mathbf{r})$ in the Hamiltonian $H_B$ to a periodic vector potential $\mathbf{A}_p(\mathbf{r})$ with a periodicity that depends on the magnetic field [84]. Using this approach, the periodicity of the magnetic superlattice resulting from the homogeneity of the magnetic field becomes apparent in the Hamiltonian.
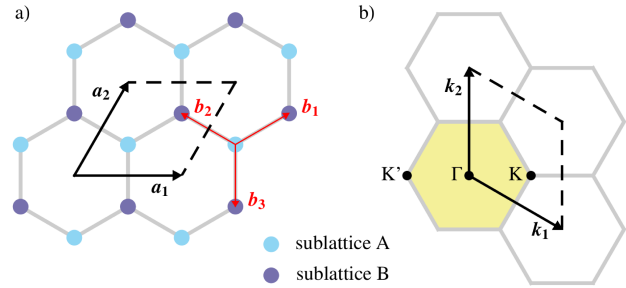


**Figure 1: Honeycomb lattice of graphene.** (a) Equivalent sublattices A and B of the two carbon atoms in the unit cell defined by the primitive lattice vectors $\mathbf{a}_1$ and $\mathbf{a}_2$. (b) Reciprocal lattice with the reciprocal lattice vectors $\mathbf{k}_1$ and $\mathbf{k}_2$, the Brillouin zone (yellow area), and the high symmetry points $\Gamma$, K, and K'.

Due to the existence of two different periodicities, each Bloch band splits up into a number of subbands, or equivalently, each Landau level splits up into different subbands with degenerate energies [60, 83, 85]. It is expedient to consider the lengths scales associated with the two periodicities, namely, the lattice constant $a_0$ and the magnetic length $l_B = \sqrt{\hbar/(e_0 B)}$. For experimentally feasible magnetic fields and typical lattice spacings the condition $a_0 \ll l_B$ applies, for example $l_B/a_0 \approx 669$ for $B = 4\,$T in graphene. In this limit it is legitimized to start with the tight-binding description of the system, since the deformation of the atomic orbitals due to the external field is negligible. Then, the magnetic field is introduced via the substitution Eq. (2) which in this context is called Peierls substitution [65, 77, 86–88]. The limit of weak magnetic fields exhibits a negligible Landau level splitting due to the crystal lattice [89], which is interpreted as the cyclotron motion of the electron not being considerably disturbed by the underlying lattice.

### 2.1.1 Electronic dispersion in Landau-quantized graphene

Graphene as a single layer of graphite is a perfect two-dimensional material consisting of carbon atoms arranged in a honeycomb lattice. The four valence electrons of each carbon atom in graphene are sp$^2$-hybridized and covalently bonded to its three neighbors. Three strong $\sigma$-bonds hold the material together and lead to the planar honeycomb lattice, while the remaining valence electron forms a $\pi$-bond. The low-energy electronic properties of graphene turn out to be captured in good approximation by a simple tight-binding approach for the $\pi$-electrons from the 2p$_z$-orbitals [7].

The Bravais lattice of graphene is hexagonal with two carbon atoms (A and B) in the unit cell, cf. Fig. 1a. The resulting honeycomb lattice is therefore comprised of two equivalent hexagonal sublattices A and B. The unit cell is spanned by the primitive lattice vectors $\mathbf{a}_1 = a_0(1, 0)$ and $\mathbf{a}_2 = a_0/2(1, \sqrt{3})$ with the lattice constant $a_0 = 0.2461$ nm [90]. The connecting vectors from a carbon atom in sublattice A to its three neighboring carbon atoms (in sublattice B) are given by $\mathbf{b}_1 = a_0/2(1, 1/\sqrt{3})$, $\mathbf{b}_2 = a_0/2(-1, 1/\sqrt{3})$, and $\mathbf{b}_3 = a_0/\sqrt{3}(0, -1)$. Fig. 1b shows the reciprocal lattice of graphene defined by the reciprocal lattice vectors $\mathbf{k}_1 = 2\pi/a_0(1, -1/\sqrt{3})$ and $\mathbf{k}_2 = 4\pi/\sqrt{3}a_0(0, 1)$. Furthermore, the first Brillouin zone (yellow area), and the high symmetry points $\boldsymbol{\Gamma} = (0, 0)$, $\mathbf{K} = 4\pi/3a_0(1, 0)$, and $\mathbf{K}' = -\mathbf{K}$ are marked in Fig. 1b.

Before the magnetic field is introduced via the Peierls substitution, an effective Hamiltonian is derived. The assumption that the relevant $\pi$-electrons are localized at the carbon sites legitimizes a tight-binding ansatz for the wave function

$$\Psi(\mathbf{r}, \mathbf{k}) = \frac{1}{\sqrt{N}} \sum_{l \in \{A, B\}} \sum_{\mathbf{R}_l} c_l(\lambda, \mathbf{k}) e^{i\mathbf{k}\cdot\mathbf{R}_l} \phi(\mathbf{r} - \mathbf{R}_l), \quad (5)$$

consisting of two parts for the two equivalent sublattices A and B with the corresponding coefficients $c_A$ and $c_B$. Here, the sum is understood to be taken over all $N$ sublattice sites $\mathbf{R}_l$ of the sublattice $l \in \{A, B\}$, and $\phi$ is the $2p_z$-orbital with an effective atomic charge $Z^* = 4.6$ [39]. The coefficients $c_l$ and the dispersion relation $\epsilon(\mathbf{k})$ are obtained by solving the Schrödinger equation $H\Psi = \epsilon\Psi$, which is achieved by multiplication (from the left) with $\Psi^*$ and integrating over $\mathbf{r}$, hence applying a scalar product $\langle\Psi(\mathbf{r})|H|\Psi(\mathbf{r})\rangle = \epsilon\langle\Psi(\mathbf{r})|\Psi(\mathbf{r})\rangle$. Introducing the spinors $= (c_A, c_B)$, a compact matrix notation is possible. Using Eq. (5) and applying the nearest-neighbor approximation, we find

$$\boldsymbol{\psi}^\dagger \begin{pmatrix} 0 & \gamma_0 e(\mathbf{k}) \\ \gamma_0 e^*(\mathbf{k}) & 0 \end{pmatrix} = \epsilon\boldsymbol{\psi}^\dagger \begin{pmatrix} 1 & s_0 \\ s_0 & 1 \end{pmatrix} \quad , \quad (6)$$

where the sum $e(\mathbf{k}) = \sum_{j=1}^{3} e^{i\mathbf{k}\mathbf{b}_j}$, as well as the integrals $\gamma_0 = \langle\phi(\mathbf{r} - \mathbf{R}_A)|H|\phi(\mathbf{r} - \mathbf{R}_{B_j})\rangle$ and $s_0 = \langle\phi(\mathbf{r})|\phi(\mathbf{r} - \mathbf{b}_1)\rangle \approx 0.07$ are defined. Here, $\gamma_0$ is independent of $j$ and corresponds to the interaction energy between carbon atoms ranging from $-2.5$ eV to $-3$ eV in graphene [90]. Furthermore, the constant integrals $\langle\phi(\mathbf{r} - \mathbf{R}_{A/B})|H|\phi(\mathbf{r} - \mathbf{R}_{A/B})\rangle$ describe an energy shift which is set to zero.

The overlap integral $s_0$ breaks the electron-hole symmetry, but its impact is negligible in the vicinities of the Dirac points (K and K' points), where the dispersion is linear in good approximation [38]. Since this article focuses

on the carrier dynamics in the low-energy regime, $s_0$ is omitted and $e(\mathbf{k})$ is expanded around the K point, using $\mathbf{k} = \xi\mathbf{K} + \mathbf{q}$ for small $\mathbf{q}$ ($|\mathbf{q}| \ll |\mathbf{K}|$), where $\xi = \pm1$ represents the K and K' point respectively (cf. Fig. 1). An expansion to first order

$$e_\xi(\mathbf{q}) \approx -\xi\frac{\sqrt{3}a_0}{2}(q_x + i\xi q_y), \quad (7)$$

yields the effective Hamiltonian which is valid in the linear region of the dispersion (for energies up to $\sim 1.5$ eV)

$$\mathcal{H}_{\boldsymbol{q}}^\xi = \xi\hbar v_F \begin{pmatrix} 0 & q_x + \xi i q_y \\ q_x - \xi i q_y & 0 \end{pmatrix}, \quad (8)$$

with the Fermi velocity in graphene $v_F = -\gamma_0 a_0\sqrt{3}/2\hbar \approx 1$ nm/fs [91].

Now, the magnetic field is introduced using the Peierls substitution $\mathbf{q} \to \boldsymbol{\pi}/\hbar$, cf. Eq. (2). To calculate the energy spectrum of the Landau levels, we define the ladder operators [65]

$$a^\dagger = \frac{l_B}{\sqrt{2}\hbar}(\pi_x + i\pi_y), \qquad \pi_x = \frac{\hbar}{\sqrt{2}l_B}\left(a^\dagger + a\right),$$
$$a = \frac{l_B}{\sqrt{2}\hbar}(\pi_x - i\pi_y), \qquad \Leftrightarrow \qquad \pi_y = -i\frac{\hbar}{\sqrt{2}l_B}\left(a^\dagger - a\right), \quad (9)$$

with the commutation relation $\left[a, a^\dagger\right] = 1$, that create and annihilate left circularly polarized quanta (quanta with an angular momentum parallel to the magnetic field), i.e. $a^\dagger|n\rangle = \sqrt{n+1}|n+1\rangle$, $a|n\rangle = \sqrt{n}|n-1\rangle$. They form the respective number operator $n = a^\dagger a$. Plugging these relations in the effective tight-binding Hamiltonian Eq. (8), where the Peierls substitution from Eq. (2) is applied first, we obtain

$$\mathcal{H}_{\boldsymbol{\pi}}^{\mathbf{K}} = \hbar\omega_c \begin{pmatrix} 0 & a^\dagger \\ a & 0 \end{pmatrix}, \quad \mathcal{H}_{\boldsymbol{\pi}}^{\mathbf{K}'} = -\hbar\omega_c \begin{pmatrix} 0 & a \\ a^\dagger & 0 \end{pmatrix}, \quad (10)$$

with the relativistic equivalent of the cyclotron frequency $\omega_c = \sqrt{2}v_F/l_B$. Defining the spinor components at the K' point in reverse order $\boldsymbol{\psi}_{\mathbf{K}'} = (c_B, c_A)$, Eq. (10) can be compactly written

$$\mathcal{H}_{\boldsymbol{\pi}}^\xi = \xi\hbar\omega_c \begin{pmatrix} 0 & a^\dagger \\ a & 0 \end{pmatrix}. \quad (11)$$

Then, the eigenvalue equation $\mathcal{H}_{\boldsymbol{\pi}}^\xi|\boldsymbol{\psi}\rangle = \epsilon|\boldsymbol{\psi}\rangle$ is readily solved

$$\epsilon_n^\lambda = \lambda\hbar\omega_c\sqrt{n} = \lambda\hbar v_F\sqrt{\frac{2ne_0 B}{\hbar}}, \quad (12)$$

$$|\boldsymbol{\psi}\rangle = \frac{\alpha_n}{\sqrt{2}}\begin{pmatrix} |n\rangle \\ \xi\lambda|n-1\rangle \end{pmatrix}, \quad \alpha_n = \begin{cases} \sqrt{2} & , n = 0 \\ 1 & , n \neq 0 \end{cases} \quad (13)$$
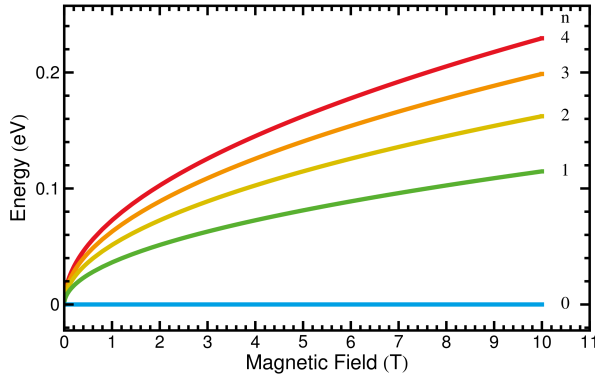
**Figure 2: Landau level spectrum.** The electronic dispersion of graphene under a homogeneous magnetic field (Eq. (12)) is shown in dependence of the magnetic field component perpendicular to the graphene plane.

where the Landau level index $n$ is defined to be a non-negative integer ($n = 0, 1, 2, \ldots$). In contrast to conventional two-dimensional electron gases with a parabolic dispersion characterized by equally spaced Landau levels, the energy of Landau levels in graphene shows a square-root dependence on the index $n$. This is a consequence of the linear electronic dispersion. Furthermore, the spacings between the Landau levels increase with the square root of the magnetic field, cf. Fig. 2. Another peculiarity of Landau-quantized graphene is the existence of a zero-energy Landau level (with $\lambda_{n=0} = 0$ by definition) which gives rise to the relativistic quantum Hall effect [55, 56].

So far, the impact of the external magnetic field on the electron's orbital degrees of freedom was discussed. Besides this interaction with the electron charge, the magnetic field also interacts with the magnetic moment due to the electron spin. This leads to a lifting of the spin-degeneracy in the Landau level spectrum (Eq. (12)) and a separation of each Landau level into two spin branches. The energy splitting $\Delta E_Z = g\mu_B B$ of electrons with opposite spins is called the Zeeman effect and depends on the material's g factor, the Bohr magneton $\mu_B = e_0\hbar/2m_0$, and the magnetic field strength $B$ [65]. Note that the direction of the magnetic field is irrelevant for the Zeeman effect, while the in-plane motion of the electrons is affected only by the perpendicular component of the magnetic field. This fact was exploited by Zhang et al. to determine an approximation for the g factor of graphene[92] $g \sim 2$, which in fact agrees with the value for the bare electron. For a typical magnetic field of $B = 4\,\text{T}$, a Zeeman splitting of $\Delta E_Z \lesssim 0.5\,\text{meV}$ is obtained. However, impurity-induced Landau level broadening is in the range of a few meV, as will be further discussed below. Therefore, assuming that the Zeeman splitting is superimposed by a larger energy broadening, we

can focus on the orbital degrees of freedom. Similarly, the lifting of the valley-degeneracy by the spin-orbit interaction is also expected to be weak in graphene [65] and will therefore be neglected.

### 2.1.2 Degeneracy of Landau levels

The cyclotron orbits located at every cell of the magnetic superlattice lead to a degeneracy of each Landau level. The latter is given by the number of electronic orbits that fit into the considered area of graphene $A$ [65, 93]. In order to calculate the Landau level degeneracy and to incorporate all magnetic degrees of freedom into the description, the motion of the electron on a cyclotron orbit is considered. In a semi-classical picture it can be described by the position operator

$$\mathbf{r} = \mathbf{X} + \boldsymbol{\eta}, \tag{14}$$

which is decomposed into the guiding center $\mathbf{X}$ and the cyclotron coordinate $\boldsymbol{\eta}$. While the latter is perpendicular to the kinetic momentum and given by $\boldsymbol{\eta} = 1/(e_0 B)(\pi_y, -\pi_x)$, the guiding center operator $\mathbf{X}$ can be related to the pseudo-momentum $\tilde{\pi}$ from Eq. (3) via $\mathbf{X} = \tilde{\pi}/(e_0 B)$. This yields the commutation relation $[X, Y] = -[\eta_x, \eta_y] = il_B^2$, showing that the components of the guiding center operator, just like the components of the kinetic momentum, are conjugate variables. Therefore, in analogy to the ladder operators defined in Eq. (9), ladder operators are defined

$$d^\dagger = \frac{1}{\sqrt{2}l_B}(iX + Y),$$
$$d = \frac{1}{\sqrt{2}l_B}(-iX + Y), \tag{15}$$

satisfying the commutation relation $\left[d, d^\dagger\right] = 1$ and forming the new number operator $m = d^\dagger d$. The eigenvalue equation

$$d^\dagger d|m\rangle = m|m\rangle \tag{16}$$

is satisfied by the eigenstates $|m\rangle$. Since the ladder operators $d^\dagger$ and $d$ commute with the Hamiltonian, the cyclotron motion may be completely characterized by the quantum numbers $n$ and $m$. Consequently, the spinor in Eq. (13) is extended to include the $m$-dependence

$$|\boldsymbol{\psi}\rangle = \frac{\alpha_n}{\sqrt{2}}\begin{pmatrix} |n, m\rangle \\ \xi\lambda|n-1, m\rangle \end{pmatrix}. \tag{17}$$

The quantum numbers in the absence of a magnetic field $q_x$ and $q_y$ are thus replaced by the quantum numbers $n$ and $m$, where $n$ is connected to the magnitude of the kinetic momentum $|\boldsymbol{\pi}| = \hbar\sqrt{2n+1}/l_B$ and $m$ expresses the position of the cyclotron orbit.

Finally, the area of a cyclotron orbit is given by the uncertainty connected with its guiding center operator $\Delta X \Delta Y = 2\pi l_B^2$, which is a result of the non vanishing commutator[65] $[X, Y] = i l_B^2$, and yields the degeneracy of each Landau level

$$N_B = \frac{A}{\Delta X \Delta Y} = \frac{A e_0 B}{2\pi\hbar}. \tag{18}$$

The quantum number $m$ may therefore assume integer values in the range $[0, N_B - 1]$.

### 2.1.3 Wave function in Landau-quantized graphene

In analogy to the case without a magnetic field, the wave function is defined as a superposition of the two sublattice wave functions from Eq. (5)

$$\Psi(\mathbf{r}) = \frac{1}{\sqrt{N}} \sum_{l \in \{A,B\}} \sum_{\mathbf{R}_l} c_l(\mathbf{R}) e^{i\xi \mathbf{K} \cdot \mathbf{R}_l} \phi(\mathbf{r} - \mathbf{R}_l). \tag{19}$$

Note that there are two main differences induced by the presence of a magnetic field:

(i) The coefficients $c_l$ are now wave functions describing the impact of the magnetic field on the motion of the charge carriers. In general, these wave functions depend on the position of the charge carriers in graphene $\mathbf{r}$. Based on the same assumption that justifies the use of the Peierls substitution, $a_0 \ll l_B$, the position-dependence of $c_l$ is restricted to lattice sites $\mathbf{R}$ in good approximation ($\mathbf{R} = \mathbf{R}_A$ without loss of generality). Then, the coefficients $c_A$ and $c_B$ are given by the spatial representation of the spinor in Eq. (17) through the relation $\langle \mathbf{R} | \boldsymbol{\psi} \rangle = (c_A, c_B)$ which yields

$$c_A(\mathbf{R}, \lambda n, m, \xi) = \frac{\alpha_n}{\sqrt{2}} \langle \mathbf{R} | n, m \rangle,$$
$$c_B(\mathbf{R}, \lambda n, m, \xi) = \frac{\alpha_n}{\sqrt{2}} \xi \lambda \langle \mathbf{R} | n-1, m \rangle. \tag{20}$$

The wave function is normalized according to $\langle \Psi(\mathbf{r}, \lambda' n', m', \xi') | \Psi(\mathbf{r}, \lambda n, m, \xi) \rangle = \delta_{\lambda,\lambda'} \delta_{n,n'} \delta_{m,m'} \delta_{\xi,\xi'}$. The explicit form of $\langle \mathbf{R} | n, m \rangle$ is given by [94]

$$\langle \mathbf{R} | n, m \rangle = i^{|n-m|} e^{-\tilde{R}^2/2} \sqrt{N_B \frac{\min(n,m)!}{\max(n,m)!}}$$
$$e^{i(n-m)\varphi} \tilde{R}^{|n-m|} L_{\min(n,m)}^{|n-m|} \left( \tilde{R}^2 \right), \tag{21}$$

with the vector $\mathbf{R} = (R, \varphi)$ in polar coordinates, the abbreviation $\tilde{R} = R/(\sqrt{2} l_B)$, and the associated Laguerre polynomials $L_n^\alpha$.

(ii) The information on the wave vector $\mathbf{q}$ (measured from the Dirac point) entering in $e^{i(\xi \mathbf{K} + \boldsymbol{\pi}/\hbar) \cdot \mathbf{R}_l}$ is lost in the magnetic field. This is an approximation which relies on

the fact that our theory only describes the region of linear dispersion around the K points, where the condition $|\mathbf{q}|/\hbar \ll |\mathbf{K}|$ certainly is satisfied. Another aspect worth mentioning in this context is that the momentum is no good quantum number in a magnetic field anymore. The modulus of the kinetic momentum $\boldsymbol{\pi}$ can be related to the Landau level index $n$, while there is an uncertainty relation between $\pi_x$ and $\pi_y$ due to their non-vanishing commutator. As a consequence, $|\boldsymbol{\pi}|$ is fixed in a specific Landau level but the direction of $\boldsymbol{\pi}$ is uncertain, hence, in $\boldsymbol{\pi}$-space Landau levels form circles around the K points. Consequently, the expectation value of the kinetic momentum is $\langle \boldsymbol{\pi} \rangle = 0$ which serves as a second way of understanding that $e^{i\boldsymbol{\pi} \cdot \mathbf{R}_l / \hbar}$ is omitted.

## 2.2 Hamilton operator and coupling matrix elements

Now, the aim is to derive a microscopic model of the carrier dynamics including the coupling of the electronic degrees of freedom with the light field driving the system out of equilibrium as well as the carrier–carrier and carrier–phonon interactions determining the relaxation dynamics of optically excited electrons. Moreover, scattering of electrons with impurities is taken into account as a broadening mechanism (pure dephasing) of the Landau level transitions. It has no direct impact on the relaxation dynamics, since the impurities can only change momenta but no energies. To take all these scattering channels into account, we define a many-particle Hamilton operator that incorporates the free-carrier part ($H_0$) as well as carrier–impurity ($H_{\text{imp}}$), carrier–light ($H_{\text{light}}$), carrier–carrier ($H_{\text{Coul}}$), and carrier phonon interactions ($H_{\text{phon}}$)

$$H = H_0 + H_{\text{imp}} + H_{\text{light}} + H_{\text{Coul}} + H_{\text{phon}}. \tag{22}$$

Introducing Heisenberg field operators $\tilde{\Psi}(\mathbf{r}) = \sum_i \Psi_i(\mathbf{r}) c_i$ and $\tilde{\Psi}^\dagger(\mathbf{r}) = \sum_i \Psi_i^\dagger(\mathbf{r}) c_i^\dagger$ for electrons and phonons, we express the many-particle Hamilton operator in second quantized language with the creation and annihilation operators $c_i^\dagger$ and $c_i$ acting on the state $i$. These operators obey the commutation relations $[c_i, c_j^\dagger]_\pm = \delta_{i,j}$ for fermionic (anti-commutator) and bosonic (commutator) particles, respectively. In the following, we denote the electronic operators as $a_i^\dagger$, $a_i$, while the phononic operators are labeled with $b_i^\dagger$, $b_i$.
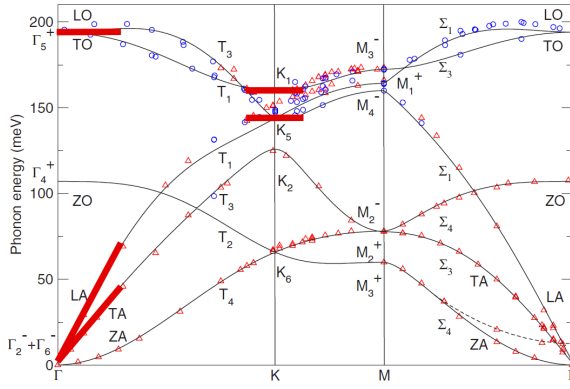
**Figure 3: Phonon dispersion of graphene.** Phonon energies $\hbar\omega_{\mathbf{p},\mu}$ are shown for of all phonon modes $\mu$ with the momentum $\mathbf{p}$ along the high-symmetry lines $\Gamma$-M-K-$\Gamma$. The red lines mark the approximated dispersions used to model the phonons included in the theory (LO, TO, LA, and TA). The figure is taken from Ref. [95]. Copyright (2007) by The American Physical Society.

### 2.2.1 Free-particle Hamiltonian

The Hamilton operator for carriers in the absence of interactions is determined by the dispersion of electrons $\epsilon_i$ and phonons $\hbar\omega_j$ and reads

$$H_0 = \sum_i \epsilon_i a_i^\dagger a_i + \sum_{\mathbf{p}\mu} \hbar\omega_{\mathbf{p}\mu}\left( b_{\mathbf{p}\mu}^\dagger b_{\mathbf{p}\mu} + \frac{1}{2} \right). \qquad (23)$$

The electronic dispersion $\epsilon_i$ has already been discussed in detail in Section 2.1.1, cf. Eq. (12). It includes the magnetic field and the compound index $i = (\lambda_i, n_i, m_i, \xi_i, s_i)$ with $\lambda_i$ denoting the band and $n_i$ the Landau level, $m_i$ describing the position of the guiding center of the cyclotron motion, while $\xi_i$ and $s_i$ are the valley and spin indices.

Fig. 3 illustrates the phonon dispersion including all six phonon modes appearing in graphene. They are divided into acoustic phonons (A) characterized by in-phase oscillations of the lattice atoms, and optical phonons (O), where the oscillation of neighboring lattice atoms is out of phase. Furthermore, a distinction is made between longitudinal (L), transverse (T), and flexural (Z) phonons. The energetically lowest Landau levels considered in this article are located in close vicinity of the Dirac points. Therefore, neglecting Umklapp processes with a momentum transfer extending beyond the Brillouin zone, the relevant phonon momenta are either small ($\Gamma$-phonons) in the case of intravalley processes, or they are $\pm\mathbf{K}$ in case of intervalley scattering (K-phonons). As will become clear when the corresponding matrix elements are evaluated, the momentum conservation, which restricts the phase space for phonon-induced scattering channels in the absence of a magnetic field, is replaced by a Gaussian factor limiting

the available phonon phase space to regions around the $\Gamma$ and the K points. In the case of optical phonons, the dispersions at the $\Gamma$ and the K point are considered to be constant in good approximation (cf. the red lines in Fig. 3), and the values $\epsilon_{\mathbf{p},\Gamma\text{TO}} = 192$ meV, $\epsilon_{\mathbf{p},\Gamma\text{LO}} = 198$ meV, $\epsilon_{\mathbf{p},\text{KTO}} = 162$ meV, and $\epsilon_{\mathbf{p},\text{KLO}} = 151$ meV [39, 96] are used. For acoustic phonons, a linear dispersion $\epsilon_{\mathbf{p},\Gamma\text{-A}} = \hbar v_{\Gamma\text{-A}} |\mathbf{p}|$ is assumed in the long-wavelength region, with $v_{\Gamma\text{LA}} = 2.308 \times 10^{-2}$ nm/fs and $v_{\Gamma\text{TA}} = 1.434 \times 10^{-2}$ nm/fs [97].

### 2.2.2 Carrier-impurity Hamiltonian

The scattering of electrons with impurities is represented by the Hamilton operator

$$H_{\text{imp}} = \sum_{i,f} D_{if} a_f^\dagger a_i, \qquad (24)$$

where $D_{if} = \int d\mathbf{r}\Psi_f^\star(\mathbf{r})U(\mathbf{r})\Psi_i(\mathbf{r})$ is the matrix element of the carrier–impurity interaction, and the Gaussian white noise potential $U(\mathbf{r})$ is used to describe randomly distributed impurities. Impurities give rise to a Landau level broadening, as will be discussed in detail in Section 2.3.1. When the broadening is smaller than the inter-Landau level spacing, the levels are well-separated and impurity-induced scattering is only possible within one single level. This results from the fact that carrier–impurity scattering is an elastic scattering mechanism, and as such does not affect the energy of individual charge carriers but only results in a Landau level broadening. While the impurity average (see for example Ref. [98]) of a single impurity potential $D_{if}$ is zero, the impurity average involving a product of two impurity potentials does not vanish (cf. Ref. [73]).

### 2.2.3 Carrier-light Hamiltonian

The interaction of electrons with the light field is treated classically. Applying the Coulomb gauge and the dipole approximation, the carrier–light Hamilton operator reads

$$H_{\text{light}} = i\hbar\frac{e_0}{m_0} \sum_{i,f} \mathbf{M}_{if} \cdot \mathbf{A}(t) a_f^\dagger a_i, \qquad (25)$$

with the elementary charge $e_0$, the electron mass $m_0$, the vector potential $\mathbf{A}(t)$ describing the incident light field, and the optical matrix element $\mathbf{M}_{if} = \int d\mathbf{r}\Psi_f^\star(\mathbf{r})\nabla\Psi_i(\mathbf{r})$. Note that the vector potential for the light field depends on time only and is considered to be spatially homogeneous, while the vector potential used to describe the magnetic field obeys only a spatial dependence. Both contribu-
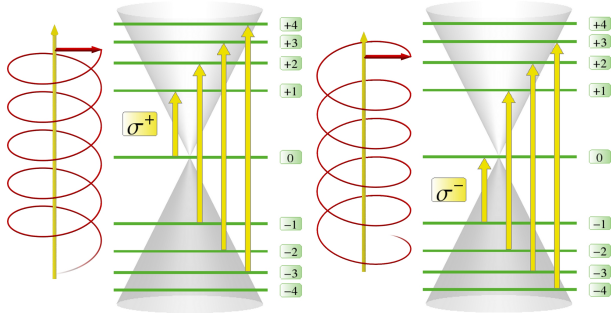
**Figure 4: Optical transitions.** The allowed optical interband transitions within the energetically lowest Landau levels are sketched.

tions are treated on a different footing which is reasonable since the physical effects of a strong magnetic field and a weak light field are dramatically different. While the former forces the electrons into cyclotron orbits and is consequently incorporated into the wave functions and the energy dispersion, the latter is considered as a perturbation of the system and thus enters the model via a scattering term. The optical matrix element can be calculated analytically within the tight-binding approach yielding [73, 99]

$$\mathbf{M}_{if} = i\delta_{\xi_i,\xi_f}\delta_{m_i,m_f}\delta_{s_i,s_f}\frac{\alpha_{n_i}\alpha_{n_f}m_0 v_F}{2\sqrt{2}\hbar}$$
$$\left[\lambda_i\hat{\boldsymbol{\epsilon}}^-\delta_{n_f,n_i-1} + \lambda_f\hat{\boldsymbol{\epsilon}}^+\delta_{n_f,n_i+1}\right] = -\mathbf{M}_{fi}^\star, \qquad (26)$$

where $\hat{\boldsymbol{\epsilon}}^\pm = (\hat{\mathbf{e}}_x \mp i\hat{\mathbf{e}}_y)/\sqrt{2}$ are Jones vectors describing left and right circularly polarized light [100]. It is convenient to define the polarization direction of light with respect to the magnetic field direction using the convention that $\sigma^+$-polarization ($\sigma^-$-polarization) means the angular momentum of the photon is parallel (anti parallel) to the magnetic field. Assuming that the direction of light propagation coincides with that of the magnetic field inducing the Landau levels (and both point into the z-direction), $\sigma^+$ and $\sigma^-$-polarized light corresponds to left ($\hat{\boldsymbol{\epsilon}}^+$) and right ($\hat{\boldsymbol{\epsilon}}^-$) circular polarization respectively, where the polarization is defined from the point of view of the receiver. The optically allowed interband transitions are sketched in Fig. 4.

The Kronecker deltas $\delta_{n_f,n_i\pm1}$ express the optical selection rules in Landau-quantized graphene allowing only transitions between Landau levels with $\Delta n = \pm1$. In Section 2.1.2, a connection was established between the quantum number $m$ and the position of the cyclotron orbit. In view of this relation, the Kronecker delta $\delta_{m_i,m_f}$ is interpreted to inhibit the optical coupling of different cyclotron orbits. This is in line with the fact that the photon momenta are negligible compared to the crystal momenta, with the result that purely optical transitions are vertical in the momentum space. The circularly polarized photons needed to excite the Landau-quantized graphene transfer an an-

gular momentum. An electron in the state $(n, m)$ has an angular momentum of $m_z = n - m$ [75]. Since the quantum number $m$ is conserved during the carrier–light interaction, the change of the Landau level index $n$ directly reflects $\Delta m_z$. Consequently, $\sigma^\pm$-polarized light corresponds to an angular momentum transfer of $\Delta m_z = \pm1$. This is in agreement with the expectation that can be deduced from the classical electron motion in a magnetic field due to the Lorentz force $\mathbf{F}_L = -e_0\mathbf{v} \times \mathbf{B}$. Note that the Rabi frequency $\Omega_{if}(t) = (e_0/m_0)\mathbf{M}_{if} \cdot \mathbf{A}(t)$ appearing in the carrier–light Hamiltonian (Eq. (25)) does not dependent on the mass of the free electron $m_0$, since the optical matrix element is proportional to $m_0$, cf. Eq. (26).

### 2.2.4 Carrier-carrier Hamiltonian

The Coulomb-induced carrier–carrier interaction is described by the Hamilton operator Eq. (22)

$$H_{\mathrm{Coul}} = \frac{1}{2}\sum_{ii'ff'}V_{ff'}^{ii'}a_f^\dagger a_{f'}^\dagger a_{i'}a_i, \qquad (27)$$

where the Coulomb matrix element in Fourier representation reads

$$V_{34}^{12} = \sum_{\mathbf{q}}V_{\mathbf{q}}\Gamma_{13}(\mathbf{q})\Gamma_{24}(-\mathbf{q}), \qquad (28)$$

with the Fourier transform $V_{\mathbf{q}} = e_0^2/(2\epsilon_0 A|\mathbf{q}|)$ of the two-dimensional Coulomb potential $V_{\mathrm{Coul}}(\mathbf{r}-\mathbf{r}') = e_0^2/(4\pi\epsilon_0|\mathbf{r}-\mathbf{r}'|)$ and the Fourier components of the electronic density $\Gamma_{if}(\mathbf{q}) = \langle\Psi_f|e^{i\mathbf{q}\mathbf{r}}|\Psi_i\rangle$, where $\epsilon_0$ is the vacuum permittivity. A concrete calculation of the matrix element $V_{34}^{12}$ yields in polar coordinates $\mathbf{q} = (q, \varphi)$

$$\begin{aligned}V_{34}^{12} =\ & \alpha_{n_1}\alpha_{n_2}\alpha_{n_3}\alpha_{n_4}\frac{e_0^2\delta_{\xi_1,\xi_3}\delta_{\xi_2,\xi_4}}{32\pi^2\epsilon_0}\int_0^\infty \mathrm{d}q\int_0^{2\pi}\mathrm{d}\varphi\\ & \times\left[\lambda_1\lambda_3 F_{n_3-1,m_3}^{n_1-1,m_1}(\mathbf{q}) + F_{n_3,m_3}^{n_1,m_1}(\mathbf{q})\right]\\ & \times\left[\lambda_2\lambda_4 F_{n_4-1,m_4}^{n_2-1,m_2}(\mathbf{q}) + F_{n_4,m_4}^{n_2,m_2}(\mathbf{q})\right], \qquad (29)\end{aligned}$$

with the form factor $F_{n,m}^{n',m'}(\mathbf{q}) = \langle n, m|e^{i\mathbf{q}\hat{\mathbf{R}}}|n', m'\rangle$ which contains the operator $e^{i\mathbf{q}\hat{\mathbf{R}}} = \frac{1}{A}\int \mathrm{d}\mathbf{R}|\mathbf{R}\rangle e^{i\mathbf{q}\mathbf{R}}\langle\mathbf{R}|$. Here, the hat is used to distinguish the operator $\hat{\mathbf{R}}$ from the position $\mathbf{R}$. Using the abbreviation $\tilde{q} = l_B q/\sqrt{2}$, the form factor reads

$$\begin{aligned}F_{n,m}^{n',m'}(\mathbf{q}) =\ & (-1)^{\Theta(n'-n)+\Theta(m'-m)}e^{-\tilde{q}^2}e^{i\varphi(n'-n-m'+m)}\\ & \times\sqrt{\frac{\min(m',m)!\min(n',n)!}{\max(m',m)!\max(n',n)!}}\tilde{q}^{|n-n'|+|m-m'|}\\ & \times L_{\min(m,m')}^{|m-m'|}\left(\tilde{q}^2\right)L_{\min(n,n')}^{|n-n'|}\left(\tilde{q}^2\right), \qquad (30)\end{aligned}$$

where the Gaussian factor $e^{-l_B^2 q^2/2}$ restricts the momentum transfers to the order of $q \sim 1/l_B$. This limits the available phase space for carrier–carrier scattering and is the equivalent to momentum conservation in the absence of a magnetic field. In a magnetic field the momentum dependence is integrated out and the matrix element $V_{34}^{12}$ is independent of **q**. A detailed examination of the form factor reveals that the angular integration in Eq. (29) yields a Kronecker delta $\delta_{n_1-m_1+n_2-m_2,n_3-m_3+n_4-m_4}$ representing the angular momentum conservation of Coulomb scattering, cf. Refs. [65] and [73] for more details on the form factor. Moreover, the Coulomb matrix element obeys the symmetry relations $V_{34}^{12} = V_{43}^{21}$, and $V_{34}^{12} = \left(V_{12}^{34}\right)^*$. Note that the electron spin has so far been neglected. Taking it into account would result in Kronecker deltas $\delta_{s_1,s_3}\delta_{s_2,s_4}$ appearing in Eq. (29) reflecting the spin conserving nature of Coulomb scattering.

Furthermore, screening of the Coulomb potential has to be introduced by substituting

$$V_{\mathbf{q}} \to \frac{V_{\mathbf{q}}}{\epsilon_{\mathrm{r}}(\mathbf{q}, \omega)} \qquad (31)$$

in Eq. (28), where the frequency $\omega$ is defined via the energy transfer of one of the two carriers involved in the scattering event $\hbar\omega = \epsilon_1 - \epsilon_3$ [101]. Here, the material-dependent relative permittivity (or dielectric function) $\epsilon_{\mathrm{r}}(\mathbf{q}, \omega) = \epsilon(\mathbf{q}, \omega)/\epsilon_0$ is the unitless ratio of the (absolute) permittivity and the vacuum permittivity. Considering a solid as a gas of electrons and positively charged ions forming a neutral plasma, the charge carriers arrange in an external electric field such that dipoles are induced damping the external field. The material is said to be polarized and the permittivity is a measure of this polarization in response to an electric field. This concept can also be applied to the material's charge carriers itself, since every charge induces an electric field. Therefore, the charge of electrons and ions in a solid is screened by all the other charges in its vicinity. The relative permittivity is composed of a constant part due to the background $\epsilon_{\mathrm{bg}}$ and a momentum-dependent part stemming from the mobile charge carriers ($\pi$-bands in graphene) and can be written as

$$\epsilon_{\mathrm{r}}(\mathbf{q}, \omega) = \epsilon_{\mathrm{bg}} \left[1 - \frac{V_{\mathbf{q}}}{\epsilon_{\mathrm{bg}}} \Pi^0(\mathbf{q}, \omega)\right], \qquad (32)$$

with the polarizability $\Pi^0(\mathbf{q}, \omega)$. The screening by the background incorporates the effects of the core states, bound electrons ($\sigma$-bands in graphene) and the surrounding environment (e.g. the substrate). For suspended graphene $\epsilon_{\mathrm{bg}} = \epsilon_{\mathrm{air}} \approx 1$ is used, while $\epsilon_{\mathrm{bg}} = (\epsilon_{\mathrm{substrate}} + \epsilon_{\mathrm{air}})/2$ is used for supported graphene where the substrate is on one side and vacuum on the other side.
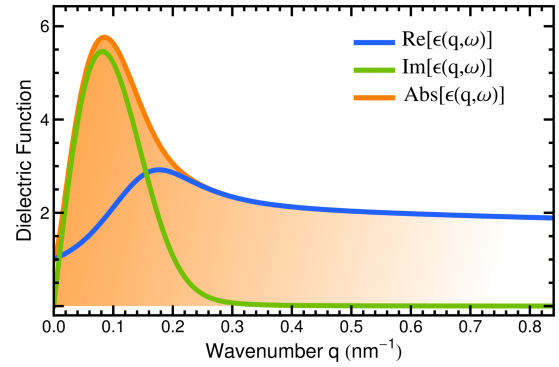


**Figure 5: Dielectric function.** Momentum dependence of the real and imaginary part as well as the absolute value of the dielectric function $\epsilon_{\mathrm{c}}(q, \omega_{01})$ for the energy transfer $\hbar\omega_{01} = \epsilon_{+1} - \epsilon_0$, and the parameters $B = 4\,\mathrm{T}$, $\mu = 0$, $T = 300\,\mathrm{K}$, and $\delta = 7\,\mathrm{meV}$. The figure is taken from Ref. [73]. Copyright (2014) by Nature Publishing Group.

The polarizability is calculated in the random phase approximation according to Goerbig et al. [65, 102, 103]

$$\Pi^0(\mathbf{q}, \omega) = 4N_B \sum_{\lambda\lambda'} \sum_{nn'} \frac{n_{\mathrm{FD}}(\epsilon_n^\lambda) - n_{\mathrm{FD}}(\epsilon_{n'}^{\lambda'})}{\epsilon_n^\lambda - \epsilon_{n'}^{\lambda'} + \hbar\omega + i\delta} \left|\tilde{F}_{\lambda n}^{\lambda' n'}(\mathbf{q})\right|^2. \qquad (33)$$

Here, $\delta$ is a broadening induced by carrier–impurity scattering which is calculated in Section 2.3.1, and $n_{\mathrm{FD}}(\epsilon) = 1/(\exp[(\epsilon - \mu)/k_B T] + 1)$ is the Fermi–Dirac distribution with the chemical potential $\mu$, the Boltzmann constant $k_B$, and the temperature $T$. The exact expression for the form factor $\tilde{F}_{\lambda n}^{\lambda' n'}(\mathbf{q})$ can be found in Ref. [65].

At a given magnetic field, Fermi energy (assuming $\epsilon_{\mathrm{F}} = \mu$), temperature, and Landau level broadening, the polarizability (Eq. 33) may be evaluated numerically for every possible energy transfer $\hbar\omega$ in dependence of the momentum transfer $q$. Fig. 5 illustrates the dielectric function for the transition $\mathrm{LL}_0 \to \mathrm{LL}_{+1}$ (for the parameters $B = 4\,\mathrm{T}$, $\mu = 0$, $T = 300\,\mathrm{K}$, and $\delta = 7\,\mathrm{meV}$). While the real part of the dielectric function closely resembles the static limit (cf. Ref. [65, 103]), the imaginary part gives a considerable contribution in the long wavelength limit. This contribution is important, since the form factor of the Coulomb interaction restricts the allowed momentum transfers $q$ to small values (cf. discussion above).

Note that, as a direct consequence of the violation of momentum conservation in a magnetic field, the vanishing screening in the long-wavelength limit $q \to 0$ does not imply divergences of the Coulomb interaction, although $V_q \propto 1/q$. In the absence of a magnetic field, momentum conservation reduces the sum over **q** in Eq. (28) to a single summand. In contrast, due to the suppression of momentum conservation in a magnetic field, here, the momentum sum has to be evaluated. It is converted into an integral in

polar coordinates $A/(2\pi)^2 \sum_{\mathbf{q}} \rightarrow \int d\mathbf{q} = \int d\varphi \int dq\, q$, and yields a factor $q$ which regularizes the divergence of $V_q$ in the limit $q \rightarrow 0$.

### 2.2.5 Carrier–phonon Hamiltonian

The carrier–phonon interaction is described by the Hamilton operator

$$H_{\text{phon}} = \sum_{if\mathbf{p}\mu} \left( g_{if}^{\mathbf{p}\mu} a_f^\dagger a_i b_{\mathbf{p}\mu} + g_{if}^{\mathbf{p}\mu^*} a_i^\dagger a_f b_{\mathbf{p}\mu}^\dagger \right), \quad (34)$$

where $g_{if}^{\mathbf{p}\mu} = \int d\mathbf{r} \Psi_f^\star(\mathbf{r}) V_{\text{phon}}^\mu(\mathbf{p}) \Psi_i(\mathbf{r})$ is the carrier–phonon matrix element with the momentum $\mathbf{p}$, the mode $\mu$ of the phonon, and the coupling potential $V_{\text{phon}}^\mu(\mathbf{p})$. The latter quantifies the interaction strength and within the nearest-neighbor approximation it can be expressed as

$$\mathbf{V}_{\text{phon}}^\mu(\mathbf{p}) = \begin{pmatrix} V_1 & V_2 \\ V_2^\star & V_1 \end{pmatrix}, \quad (35)$$

which is obtained in a continuum model for long-wavelength phonons. It incorporates the coupling of electrons to phonons via a scalar deformation potential $V_1$ as well as bond-length modulations $V_2$ (modulated hopping) [104–107]. While the deformation potential describes an on-site coupling, where the initial and final electronic states are located on the same lattice site, the modulated hopping term couples electronic states on neighboring sites.

Overall, the coupling matrices for acoustic and optical phonons are expressed in terms of the phonon momentum transfer in polar coordinates $\mathbf{p} = (p, \varphi_{\mathbf{p}})$, the displacement vector in polar coordinates $\mathbf{u} = (u, \varphi_{\mathbf{u}})$, and the angles $\varphi_{\mathbf{p},\mathbf{u}}^\pm = \varphi_{\mathbf{p}} \pm \varphi_{\mathbf{u}}$:

$$\mathbf{V}_{\text{phon}}^{\text{ac}}(\mathbf{p}) = ip D_{\mathbf{p}}^\mu \begin{pmatrix} g_1 \cos\varphi_{\mathbf{p},\mathbf{u}}^- P & g_2 e^{-i\xi\varphi_{\mathbf{p},\mathbf{u}}^+} P \\ -g_2 e^{i\xi\varphi_{\mathbf{p},\mathbf{u}}^+} P^\star & g_1 \cos\varphi_{\mathbf{p},\mathbf{u}}^- P \end{pmatrix}, \quad (36)$$

$$\mathbf{V}_{\text{phon}}^{\text{opt}}(\mathbf{p}) = i\xi \frac{\sqrt{2}3\beta\hbar v_F}{a_0^2} D_{\mathbf{p}}^\mu \begin{pmatrix} 0 & -e^{i\xi\varphi_{\mathbf{u}}} P \\ e^{-i\xi\varphi_{\mathbf{u}}} P^\star & 0 \end{pmatrix}, \quad (37)$$

where $g_1 = 16$ eV [108] is the deformation potential, $g_2 = -\sqrt{3}\kappa\beta\hbar v_F/2a_0 \approx -1.5$ eV is the potential describing the modulated hopping amplitude for acoustic phonons including the parameters $\beta = -d\ln\gamma_0/d\ln|\mathbf{b}_j| \approx 2$ and $\kappa \approx 1/3$ [105], $P = e^{i\mathbf{p}\mathbf{R}}$ is the plane wave factor, and $D_{\mathbf{p}}^\mu = \sqrt{\hbar/MA\omega_{\mathbf{p}\mu}}$ is a prefactor depending on the graphene mass density $M = 7.6 \times 10^{-8}$ gcm$^{-2}$ [39], the area of graphene $A$, and the phonon energy $\omega_{\mathbf{p}\mu}$.

The deformation potential coupling $g_1$ is about one order of magnitude larger than the modulated hopping

strength $g_2$ and provides the dominant contribution for longitudinal acoustic phonons (where $\cos(\varphi_{\mathbf{p},\mathbf{u}}^{\text{long}} = 0) = 1$). In the case of transverse acoustic phonons, the modulated hopping becomes important, since here the deformation potential coupling vanishes, that is $\cos(\varphi_{\mathbf{p},\mathbf{u}}^{\text{trans}} = \pi/2) = 0$. Note that the deformation potential is subject to electronic screening, which is particularly strong for small wave vectors [104]. In contrast, the modulated hopping giving rise to the important interaction with optical phonons is not affected by screening.

Finally, the carrier–phonon matrix element is calculated using the coupling potential of the respective mode $\mathbf{V}_{\text{phon}}$ (Eqs. 36–37), and the spinor representation of the wave function

$$(\mathbf{R}, \lambda n, m, \xi) = \frac{1}{\sqrt{A}} e^{i\xi\mathbf{K}\cdot\mathbf{R}} \begin{pmatrix} c_A(\mathbf{R}, \lambda n, m, \xi) \\ c_B(\mathbf{R}, \lambda n, m, \xi) \end{pmatrix}. \quad (38)$$

It yields for acoustic phonons

$$\left| g_{if}^{\mathbf{p}, \Gamma\text{LA}} \right|^2 = \frac{\alpha_{n_i}^2 \alpha_{n_f}^2 \hbar p}{4MA v_{\Gamma\text{LA}}} \left| \xi\lambda_i g_2 e^{-2i\xi\varphi_{\mathbf{p}}} F_{n_f,m_f}^{n_i-1,m_i}(\mathbf{p}) \right.$$
$$- \xi\lambda_f g_2 e^{2i\xi\varphi_{\mathbf{p}}} F_{n_f-1,m_f}^{n_i,m_i}(-\mathbf{p})$$
$$\left. + g_1 \left[ F_{n_f,m_f}^{n_i,m_i}(\mathbf{p}) + \lambda_i\lambda_f F_{n_f-1,m_f}^{n_i-1,m_i}(\mathbf{p}) \right] \right|^2, \quad (39)$$

$$\left| g_{if}^{\mathbf{p}, \Gamma\text{TA}} \right|^2 = \frac{\alpha_{n_i}^2 \alpha_{n_f}^2 \hbar p}{4MA v_{\Gamma\text{-A}}} \left| \lambda_f g_2 e^{2i\xi\varphi_{\mathbf{p}}} F_{n_f-1,m_f}^{n_i,m_i}(-\mathbf{p}) \right.$$
$$\left. + \lambda_i g_2 e^{-2i\xi\varphi_{\mathbf{p}}} F_{n_f,m_f}^{n_i-1,m_i}(\mathbf{p}) \right|^2, \quad (40)$$

and for optical phonons

$$\left| g_{if}^{\mathbf{p}, \Gamma\text{-O}} \right|^2 = \frac{\alpha_{n_i}^2 \alpha_{n_f}^2 9\beta^2 \hbar^4 v_F^2}{2a_0^4 MA\epsilon_{\mathbf{p},\Gamma\text{-O}}} \left| \lambda_f e^{-i\xi\varphi_{\mathbf{p}}} F_{n_f-1,m_f}^{n_i,m_i}(-\mathbf{p}) \right.$$
$$\left. \pm \lambda_i e^{i\xi\varphi_{\mathbf{p}}} F_{n_f,m_f}^{n_i-1,m_i}(\mathbf{p}) \right|^2, \quad (41)$$

$$\left| g_{if}^{\mathbf{p},\text{K-O}} \right|^2 = \alpha_{n_i}^2 \alpha_{n_f}^2 \left\langle g_{\text{K-O}}^2 \right\rangle_{\text{DFT}}$$
$$\times \left| \lambda_f F_{n_f-1,m_f}^{n_i,m_i}(-\mathbf{p}) - \lambda_i F_{n_f,m_f}^{n_i-1,m_i}(\mathbf{p}) \right|^2, \quad (42)$$

where the + sign refers to the transverse mode ($\Gamma$TO) and the − sign to the longitudinal mode ($\Gamma$LO). While analytic expressions are obtained in the case of $\Gamma$ phonons, the carrier–phonon interaction strengths $\left\langle g_{\text{KTO}}^2 \right\rangle_{\text{DFT}} = 0.0994$ eV$^2 \cdot A_{\text{uc}}/A$, and $\left\langle g_{\text{KLO}}^2 \right\rangle_{\text{DFT}} = 0.00149$ eV$^2 \cdot A_{\text{uc}}/A$ are based on numerical calculations within density functional theory (DFT) that where performed by Piscanec et al. [109]. Here, $A_{\text{uc}} = \sqrt{3}a_0^2/2$ is the unit cell area and $A$ is the area of graphene which cancels after performing the momentum sum in the scattering rates. The DFT calculations yield phonon dispersion relations showing Kohn anomalies [110] that manifest itself by sharp kinks at high symmetry points in the Brillouin zone. Then, the carrier–phonon

interaction strengths can be deduced from the slopes of these kinks as was analytically proven in the same work (Ref. [109]). Note that the interaction strengths in the case of the $\Gamma$ phonons are also in agreement with the corresponding DFT calculations [109]. Finally, the form factors $F_{n,m}^{n',m'}(\mathbf{p})$ are the same as in the case of Coulomb scattering. Since a phonon can absorb (or provide) any angular momentum, there are no selection rules for the carrier–phonon interaction and restrictions of the corresponding scattering channels are only imposed by the energy conservation.

## 2.3 Microscopic Bloch equations for Landau-quantized graphene

Knowing the full many-particle Hamilton operator including all matrix elements, the temporal evolution of an arbitrary operator $\mathcal{O}$ can be derived using the Heisenberg equation of motion $i\hbar\frac{\mathrm{d}}{\mathrm{d}t}\mathcal{O}(t) = [\mathcal{O}, H]$ [38, 111]. Employed on the quantities of interest, the microscopic polarization $p_{if}(t) = \langle a_f^\dagger a_i \rangle(t)$, and the population probability $\rho_i(t) = \langle a_i^\dagger a_i \rangle(t)$, this approach yields the Bloch equations for Landau-quantized graphene[73]. While the polarization $p_{if}$ is a measure of the optically–induced transition probability from the initial $i$ to the final state $f$, $\rho_i$ is the occupation of state $i$ which is given by the Fermi–Dirac distribution in equilibrium.

In the subsequent sections, the contributions to the Bloch equations stemming from the different parts of the Hamiltonian (Eq. (22)) are investigated. One distinguishes the single particle contributions ($H_0$, $H_{\mathrm{imp}}$, $H_{\mathrm{light}}$), where the set of Heisenberg equations of motion is closed, from the many-particle contributions ($H_{\mathrm{Coul}}$, $H_{\mathrm{phon}}$) which are characterized by the emergence of an infinite hierarchy of equations. In the latter case, the temporal derivative of a two-operator expectation value (e.g. $\dot{p}_{if}$, $\dot{\rho}_i$) couples to a higher-order expectation value, such as $C = \langle a_1^\dagger a_2^\dagger a_3 a_4 \rangle$, which itself has a temporal derivative that couples to the next higher order, and so on. To obtain a finite set of equations in the case of a many-particle interaction, the hierarchy is truncated exploiting a correlation expansion [112].

Besides the need to truncate a finite hierarchy of equations, the Bloch equations for many-particle interactions may further be simplified by applying the Markov approximation which is a scheme to solve a differential equation of the form

$$\frac{\mathrm{d}}{\mathrm{d}t}x(t) = (i\Delta\omega - \gamma)x(t) + iQ(t), \tag{43}$$

with a frequency difference $\Delta\omega$, a damping $\gamma$, and a function $Q(t)$, which typically involves higher-order correla-

tions with respect to the quantity of interest $x(t)$. A simple solution is achieved by neglecting the memory kernel of $Q(t)$, which yields

$$\mathrm{Im}\left[x(t)\right] = i\pi Q(t)L_\gamma(\Delta\omega), \tag{44}$$

where $L_\gamma(\Delta\omega)$ is a Lorentzian with the broadening $\gamma$. In the limit of a vanishing damping $\gamma$, the Lorentzian becomes a Dirac delta function reflecting the strict energy conservation. Since Landau-quantized graphene is a system with discrete energy levels (cf. Eq. (12)), the limit of a vanishing damping is not applied here. Instead, a finite damping $\gamma$ is considered which is equivalent to the Landau level broadening, and can be caused by disorder [113], or alternatively by interaction with acoustic phonons [114, 115]. Therefore, before the many-particle dynamics of the charge carriers is accessible, the impurity-induced Landau level broadening is determined in the next section. Here, we also include the contributions of the other single-particle terms to the Bloch equations for Landau-quantized graphene.

### 2.3.1 Single-particle contributions

To calculate the Landau level broadening, electron-impurity scattering is taken into account in a self-consistent Born approximation which was developed by Ando and Uemura in the Green's function formalism [113], and was later transferred to the density matrix approach [73]. The starting point is the equation of motion for the impurity average of the microscopic polarization $\overline{p_{if}}$ taking into account the contributions $H_0$, $H_{\mathrm{imp}}$, and $H_{\mathrm{light}}$ in the Hamiltonian (Eq. (22))

$$H = \sum_i \epsilon_i a_i^\dagger a_i + \sum_{\mathbf{p}\mu} \hbar\omega_{\mathbf{p}\mu}\left(b_{\mathbf{p}\mu}^\dagger b_{\mathbf{p}\mu} + \frac{1}{2}\right)$$
$$+ \sum_{v,v'} D_{vv'} a_{v'}^\dagger a_v + i\hbar\sum_{l,l'}\Omega_{ll'}(t)a_{l'}^\dagger a_l. \tag{45}$$

The impurity average constitutes a new correlation — besides the correlation stemming from the expectation value — and also requires at least a classical correlation expansion. An expansion to the lowest order reads

$$\dot{\overline{\rho_i}} = -2\sum_l \mathrm{Re}\left[\Omega_{il}\overline{p_{il}}\right], \tag{46}$$

$$\dot{\overline{p_{if}}} = i\triangle\omega_{if}\overline{p_{if}} + \left(\overline{Dp}\right)_{if} + \Omega_{if}^\star\left(\overline{\rho_i} - \overline{\rho_f}\right), \tag{47}$$

with the impurity averaged quantities $\overline{\rho_i}$, $\overline{p_{if}}$ involving the averaged products of $D_{if}$ and $p_{if}$

$$\left(\overline{Dp}\right)_{if}(t) = \frac{i}{\hbar}\frac{1}{N_B}\sum_m\sum_v\left[\overline{D_{fv}p_{iv}} - \overline{D_{vi}p_{vf}}\right]. \tag{48}$$

Here, the energy difference $\triangle\omega_{if} = (\epsilon_f - \epsilon_i)/\hbar$ is responsible for the oscillation of the microscopic polarization $p_{if}$ due to the free energy part of the Hamiltonian. For a non-zero electromagnetic radiation field $\mathbf{A}(t)$, the Rabi frequency $\Omega_{if}(t) = (e_0/m_0)\mathbf{M}_{if} \cdot \mathbf{A}(t)$ of an optically allowed transition $i \to f$ induces a buildup of the polarization (cf. Eq. (47)) resulting in an occupation change (cf. Eq. (46)). Therefore, the lowest order of excitation is fully covered by the dynamics of the polarization, which is called the linear optics regime. Within this regime, it is possible to solve the differential equations Eqs. (47), (46) in the frequency domain. Holding the occupations $\overline{\rho_j}$ constant, the solution depends only on $\left(\overline{Dp}\right)_{if}(\omega)$. This is readily obtained via a Fourier transform from the equation of motion of $\left(\overline{Dp}\right)_{if}$, where a phenomenological damping term is introduced first [73]. Then, the system of equations consisting of $\overline{p_{if}}(\omega)$ and $\left(\overline{Dp}\right)_{if}(\omega)$ is solved and allows to calculate the impurity induced dephasing

$$\gamma_{if}^{\text{imp}} \approx \frac{v_{\text{F}}}{l_B \sqrt{A_{\text{imp}}}} \tag{49}$$

in a self-consistent second-order Born approximation, with the dimensionless parameter $A_{\text{imp}}$ introduced by Shon and Ando, cf. Ref. [116], that defines the impurity potential scattering strength. Finally, replacing the term $\left(\overline{Dp}\right)_{if}$ in Eq. (47) with $-\gamma_{if}^{\text{imp}}\overline{p_{if}}$, the impurity-induced dephasing is incorporated into the optical Bloch equations yielding

$$\dot{\rho}_i = -2 \sum_l \text{Re}\left[\Omega_{il}p_{il}\right], \tag{50}$$

$$\dot{p}_{if} = \left(i\triangle\omega_{if} - \gamma_{if}^{\text{imp}}\right) p_{if} + \Omega_{if}^{\star}\left(\rho_i - \rho_f\right), \tag{51}$$

where bars indicating the impurity average were omitted for reasons of clarity.

Note that $\Sigma = i\hbar\gamma_{if}^{\text{imp}}/2$ can be interpreted as the self-energy of the Green function $G = (E - H - \Sigma)^{-1}$, from which the density of states (DOS) can be deduced (see for example [117]), and reads

$$\text{DOS}(E) = \frac{2N_B}{\pi\hbar\gamma_{if}^{\text{imp}}} \sqrt{1 - \left(\frac{E}{2\hbar\gamma_{if}^{\text{imp}}}\right)^2}, \tag{52}$$

which allows to extract the full width $\Gamma_{\text{FW}} = 4\hbar\gamma_{if}^{\text{imp}}$ of the broadened Landau levels, as illustrated in Fig. 6.

In addition to the Landau level broadening induced by impurity scattering which is discussed in this section, impurities can also cause a spatial charge inhomogeneity [118, 119]. This is expected to further increase the Landau level broadening. However, since the parameter $A_{\text{imp}}$ is chosen to yield broadenings that agree with experimental values, the contribution of spacial charge inhomogeneities has been implicitly considered.
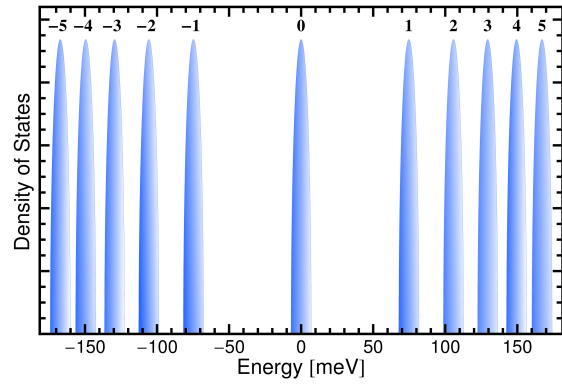


**Figure 6: Density of states.** DOS of the energetically lowest Landau levels as obtained in a self-consistent Born approximation for an impurity scattering parameter $A_{\text{imp}} = 200$ at a magnetic field of $B = 4$ T. The Figure is taken from Ref. [73] Copyright (2014) by Nature Publishing Group.

### 2.3.2 Many-particle contributions

The lowest order terms in the equations of motion for the many-particle carrier–carrier and carrier–phonon interactions are the mean field contributions corresponding to the Hartree–Fock approximation. They give rise to a renormalization of the energy and of the Rabi frequency resulting in excitonic effects [39]. Since these effects are known to be negligible in the low-energy limit near the Dirac points of graphene [39, 120, 121], we focus on the terms in second-order correlation expansion which describe two-particle scattering processes.

Setting up the Heisenberg equations of motion and exploiting the Markov approximation (Eqs. (43), (44)), the contributions to the Bloch equations stemming from carrier–carrier and carrier–phonon scattering are obtained [73]:

$$\dot{\rho}_i = S_i^{\text{in}}\left(1 - \rho_i\right) - S_i^{\text{out}}\rho_i, \tag{53}$$

$$\dot{p}_{if} = -\frac{1}{2}\left(S_i^{\text{in}} + S_i^{\text{out}} + S_f^{\text{in}} + S_f^{\text{out}}\right) p_{if}, \tag{54}$$

with the time dependent scattering rates for carrier–carrier

$$S_j^{\text{in/out}}(t)\Big|_{\text{Coul}} = \frac{2\pi}{\hbar} \sum_{abc} \tilde{V}_{bc}^{ja} f_{abc}^{\text{in/out}} L_\Gamma\left(\triangle E_{jabc}\right), \tag{55}$$

and for carrier–phonon scattering

$$S_j^{\text{in/out}}(t)\Big|_{\text{phon}} = \frac{2\pi}{\hbar} \sum_{a\mathbf{p}\mu} \left|\tilde{g}_{aj}^{\mathbf{p}\mu}\right|^2 f_{aj}^{\text{in/out}}. \tag{56}$$

In these scattering equations, compound indices are used $a = (\lambda_a, n_a)$, including the band index $\lambda_a$, and the Landau level index $n_a$. The sums over the index connected to the

guiding center of the cyclotron motion $m_a$, the valley index $\xi_a$, and the spin index $s_a$ have already been performed assuming that neither the occupations nor the polarizations depend on the quantum number $m$ due to the homogeneity of space. While the carrier–phonon scattering is determined by $\left|\tilde{g}_{ab}^{\mathbf{p}\mu}\right|^2 = \frac{1}{N_B}\sum_{m_a m_b}\left|g_{ab}^{\mathbf{p}\mu}\right|^2$, the interaction strength of the carrier–carrier scattering is given by the sum $\tilde{V}_{cd}^{ab} = \frac{1}{N_B}\sum_{m_a m_b m_c m_d} V_{cd}^{ab}\left(4V_{ab}^{cd} - V_{ab}^{dc}\right)$ which consists of the direct (first term) and the exchange (second term) contribution. Since the phenomenological introduction of dynamical screening according to Eq. (31) is only applicable to the direct term, we neglect the exchange term and thereby employ the shielded potential approximation [101]. Furthermore, the terms

$$f_{abc}^{\text{in}} = (1 - \rho_a)\rho_b\rho_c, \tag{57}$$

$$f_{abc}^{\text{out}} = \rho_a (1 - \rho_b)(1 - \rho_c) \tag{58}$$

in Eq. (55) describe the Pauli blocking in the Coulomb interaction. In the case of phonon-induced scattering, the terms

$$f_{aj}^{\text{in}} = \rho_j \left[(n_{\mathbf{p}\mu} + 1)L_\Gamma\left(\triangle E_{ja\mu}^{\text{em}}\right) + n_{\mathbf{p}\mu}L_\Gamma\left(\triangle E_{ja\mu}^{\text{ab}}\right)\right], \tag{59}$$

$$f_{aj}^{\text{out}}(1 - \rho_a)\left[(n_{\mathbf{p}\mu} + 1)L_\Gamma\left(\triangle E_{aj\mu}^{\text{em}}\right) + n_{\mathbf{p}\mu}L_\Gamma\left(\triangle E_{aj\mu}^{\text{ab}}\right)\right] \tag{60}$$

describe the emission and absorption of phonons. Both Coulomb- and phonon-induced scattering rates include the Lorentzian

$$L_\Gamma(\triangle E) = \frac{\Gamma}{\pi\left(\triangle E^2 + \Gamma^2\right)}, \tag{61}$$

which reflects the energy conservation and appears as a result of the non-vanishing impurity-induced Landau level broadening $\Gamma = \hbar\gamma^{\text{imp}}$ that is assumed to constitute the dominant dephasing term. Moreover, the phonon occupation $n_{\mathbf{p}\mu}$, the energy difference for carrier–carrier scattering $\triangle E_{ff'}^{ii'} = \epsilon_f - \epsilon_i + \epsilon_{f'} - \epsilon_{i'}$, and the energy differences $\triangle E^{\text{em/ab}} = \epsilon_f - \epsilon_i \pm \epsilon_{\mathbf{p},\mu}$ for the emission (+) and absorption (–) of a phonon were introduced. The dynamics of the phonon occupations is not calculated, but the $n_{\mathbf{p}\mu}$'s are considered to be in equilibrium with a bath, and hence given by the Bose–Einstein distribution.

# 3 Ultrafast carrier dynamics

In this section, we investigate the ultrafast dynamics of photo-excited charge carriers, where the optical excitation is described by Eqs. (50)-(51), and the many-particle scat-

tering is included via Eqs. (53)-(54). The optical pulse is expressed via the time-dependent part of the vector potential

$$\mathbf{A}(t) = A_{\text{env}}(t)\left[A_0^+\begin{pmatrix}\cos\omega t\\\sin\omega t\end{pmatrix} + A_0^-\begin{pmatrix}\cos\omega t\\-\sin\omega t\end{pmatrix}\right], \tag{62}$$

which possesses a $\sigma^+$ and a $\sigma^-$-polarized contribution with the corresponding amplitudes $A_0^+$ and $A_0^-$, respectively. Since $\sigma^+$ and $\sigma^-$-polarized light excites different inter-Landau level transitions, cf. Fig. 4, we investigate the corresponding contributions separately. Then, combining both contributions, an excitation pulse of an arbitrary polarization (circular, linear, or elliptical) can be constructed. It is expedient to define $A_0^\pm \in \{0, 1\}$, which allows to express the amplitude of the Gaussian envelope function in terms of experimentally accessible parameters: (i) energy transfer per unit area called pump fluence $\epsilon_{\text{pf}}$, and (ii) the full width at half maximum (FWHM) of the pulse intensity $\sigma_{\text{FWHM}}^{\text{exp}}$. Under the assumption that the pulse width is much larger than its period $T = 2\pi/\omega$, this yields

$$A_{\text{env}}(t) = \frac{1}{\omega}\sqrt{\frac{2\sqrt{\ln 2}\,\epsilon_{\text{pf}}}{\sqrt{\pi}\epsilon_0 c\,\sigma_{\text{FWHM}}^{\text{exp}}}}e^{-\frac{2\ln 2\,t^2}{(\sigma_{\text{FWHM}}^{\text{exp}})^2}}. \tag{63}$$

Another characterization of the optical excitation strength is the pulse area $\Theta_{if} = 2\int_{-\infty}^{\infty}dt'\left|\Omega_{if}^{\text{env}}(t')\right|$, where $\Omega_{if}^{\text{env}}$ is the envelope of the Rabi frequency. The area $\Theta_{if}$ provides an effective pumping strength, since it determines the final values of $p_{if}$, $\rho_f$, and $\rho_i$ after the pump pulse, if no dephasing of the polarization is present, and it reads

$$\begin{aligned}\Theta_{if} &= \delta_{\xi_i,\xi_f}\delta_{m_i,m_f}\frac{\alpha_{n_i}\alpha_{n_f}e_0 v_{\text{F}}}{2\hbar\triangle\omega_{if}}\sqrt{\frac{\sqrt{\pi}\,\epsilon_{\text{pf}}\sigma_{\text{FWHM}}^{\text{exp}}}{\sqrt{\ln 2}\,\epsilon_0 c}}\\&\quad\times\left[\lambda_i A_0^-\delta_{n_f,n_i-1} + \lambda_f A_0^+\delta_{n_f,n_i+1}\right].\end{aligned} \tag{64}$$

In the absence of a dephasing, a pulse with the area $\Theta_{if} = \pi$ effects a complete inversion of the occupations, while a pulse with the area $\Theta_{if} = 2\pi$ reconstitutes the initial conditions of $p_{if}$, $\rho_f$, and $\rho_i$. The pump-induced occupation change increases with an increasing fluence and width of the pulse, however it scales inversely with the resonance energy of the transition, cf. Eq. (64).

Fig. 7a illustrates the x-component of a circularly polarized excitation pulse ($\sigma^+$-polarized) with typical values for the pump fluence ($\epsilon_{\text{pf}} = 0.14\,\mu\text{Jcm}^{-2}$), width ($\sigma_{\text{FWHM}}^{\text{exp}} = 1\,\text{ps}$), and an excitation energy which is in resonance with the inter-Landau level transition $\text{LL}_{-1} \to \text{LL}_{+2}$ (175 meV at $B = 4\,\text{T}$). The slowly varying Gaussian envelope function $A_{\text{env}}(t)$ (cf. thick orange line in Fig. 7a) is modulated by a fast oscillation with the period $T \approx 24fs$ (cf. thin yellow

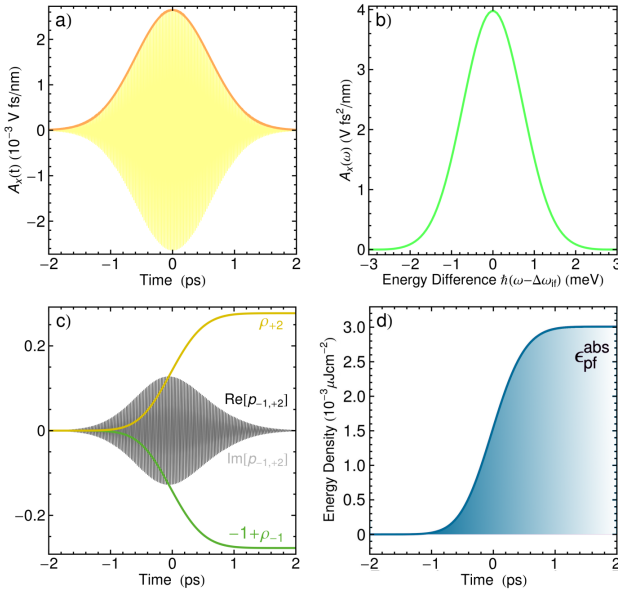**Figure 7: Optical excitation pulse.** Temporal evolution (a) and Fourier transform (b) of the x-component of $\mathbf{A}(t)$ for a $\sigma^+$-polarized excitation pulse with a pump fluence $\epsilon_{\mathrm{pf}} = 0.14\,\mu\mathrm{Jcm}^{-2}$, a width $\sigma_{\mathrm{FWHM}}^{\mathrm{exp}} = 1\,\mathrm{ps}$, and an excitation energy of 175 meV which is in resonance with the inter-Landau level transition $\mathrm{LL}_{-1} \to \mathrm{LL}_{+2}$ at $B = 4\,\mathrm{T}$. The thick orange line in (a) represents the Gaussian envelope of the pulse. Furthermore, the occupations $\rho_{-1}(t)$ and $\rho_{+2}(t)$ as well as the polarization $p_{-1,+2}(t)$ are illustrated (c), and the increase of the energy density corresponding to the absorbed pump fluence $\epsilon_{\mathrm{pf}}^{\mathrm{abs}}$ is shown (d).

line in Fig. 7a) which is due to the cosine in Eq. (62). The spectrum of this exemplary pulse is narrow compared to the Landau level spacings, cf. Fig 7b, and is of the same order as the impurity-induced level broadening, cf. Eq. (49). Therefore, pulsed excitations of Landau-quantized graphene on picosecond timescales can be used to address specific transitions between Landau levels and the pumping of off-resonant transitions may be neglected. The dynamics of the occupations as well as the polarization, involved when the transition $\mathrm{LL}_{-1} \to \mathrm{LL}_{+2}$ is optically excited, are shown in Fig. 7c. The polarization oscillates with the transition frequency $\triangle\omega_{-1,+2}$, it has an envelope function resembling that of the excitation pulse, and it shows a phase shift of $\pi/2$ between the real and the imaginary part. At the same time charge carriers are excited from $\mathrm{LL}_{-1}$ (decrease of $\rho_{-1}$) to $\mathrm{LL}_{+2}$ (increase of $\rho_{+2}$). While the polarization decays after the optical excitation due to the impurity-induced dephasing (cf. $\gamma_{if}^{\mathrm{imp}}$ in Eq. (51)), the occupations remain constant after the pump pulse, since many-particle scattering acting during and in particular after the pulse is not included so far. The increase of the energy density during the optical excitation is illustrated in Fig. 7d. The amount of energy density increase ($3.1 \cdot 10^{-3}\,\mu\mathrm{Jcm}^{-2}$)
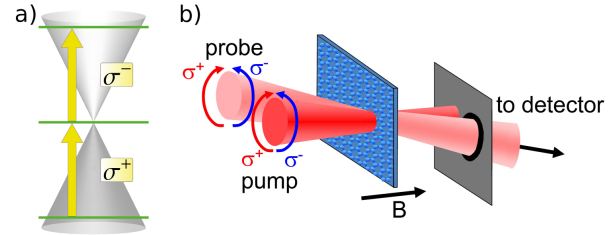


**Figure 8: Circularly polarized differential transmission spectroscopy.** Sketch of the possible optical transitions of the energetically lowest Landau levels $\mathrm{LL}_{-1}$, $\mathrm{LL}_0$ and $\mathrm{LL}_{+1}$ (a), and the experimental setup to measure the differential transmission (b). Figure (b) is taken from Ref. [70] Copyright (2015) by Nature Publishing Group.

corresponds to the absorbed pump fluence with $\epsilon_{\mathrm{pf}}^{\mathrm{abs}} \approx 0.022\epsilon_{\mathrm{pf}}$. It is smaller than the pump fluence of the excitation pulse $\epsilon_{\mathrm{pf}}$ since one layer of graphene absorbs only a fraction of the incoming radiation. The obtained ratio of absorbed to applied pump fluence of 2.2% is in good agreement with the experimentally observed value [122].

The semi classical description of the carrier–light interaction considered so far captures the Rabi oscillations comprising of the optical excitation as well as the stimulated emission. However, the spontaneous emission leading to a radiative decay is not included, since it occurs on a longer time scale compared to the dynamics discussed here. To demonstrate this, the radiative decay rate is approximated using a simple approach based on Fermi's golden rule [123]

$$\Gamma_{if} = \frac{\pi\hbar e_0^2}{\epsilon_0 V m_0^2} \sum_{\mathbf{k}\sigma} \frac{1}{\omega_{\mathbf{k}}} \left| \epsilon^\sigma \cdot \mathbf{M}_{if} \right|^2 \delta(\Delta\omega_{if} - \omega_{\mathbf{k}}), \qquad (65)$$

where the sample is assumed to be in a cavity with volume $V$. Here, $\mathbf{k}$ is the wave vector, $\omega_{\mathbf{k}} = c|\mathbf{k}|$ is the angular frequency of a photon, and $\boldsymbol{\epsilon}^\sigma$ is the polarization vector for circularly polarized light. Assuming an infinite volume $V$, the $\mathbf{k}$-sum can be transformed into an integral ($\sum_{\mathbf{k}} \to V/(8\pi^3) \int d\mathbf{k}$), and, using the expression for the optical matrix element (Eq. (26)), one finds

$$\Gamma_{if} = \left(\alpha_{n_i}\alpha_{n_f} e_0 v_{\mathrm{F}}\right)^2 \left(\frac{n_{\mathrm{bg}}}{c}\right)^3 \frac{\Delta\omega_{if}}{16\pi\hbar\epsilon_0}, \qquad (66)$$

where a correction of the vacuum light velocity due to the background refractive index $n_{\mathrm{bg}} = \sqrt{\epsilon_{\mathrm{bg}}}$ is introduced through $c \to c/n_{\mathrm{bg}}$. For reasons of clarity, the Kronecker deltas $\delta_{\xi_i,\xi_f}\delta_{m_i,m_f}\delta_{n_f,n_i\pm1}$ were omitted, hence, we have to keep in mind that spontaneous emission can only occur for optically allowed transitions (cf. Eq. (26)). This yields the radiative decay time $\tau_{+2,-1} = \Gamma_{+2,-1}^{-1} \approx 28\,\mathrm{ns}$ for the transition $\mathrm{LL}_{+2} \to \mathrm{LL}_{-1}$ in Landau-quantized graphene on a SiC substrate. Therefore, considering the ultrafast carrier dy-
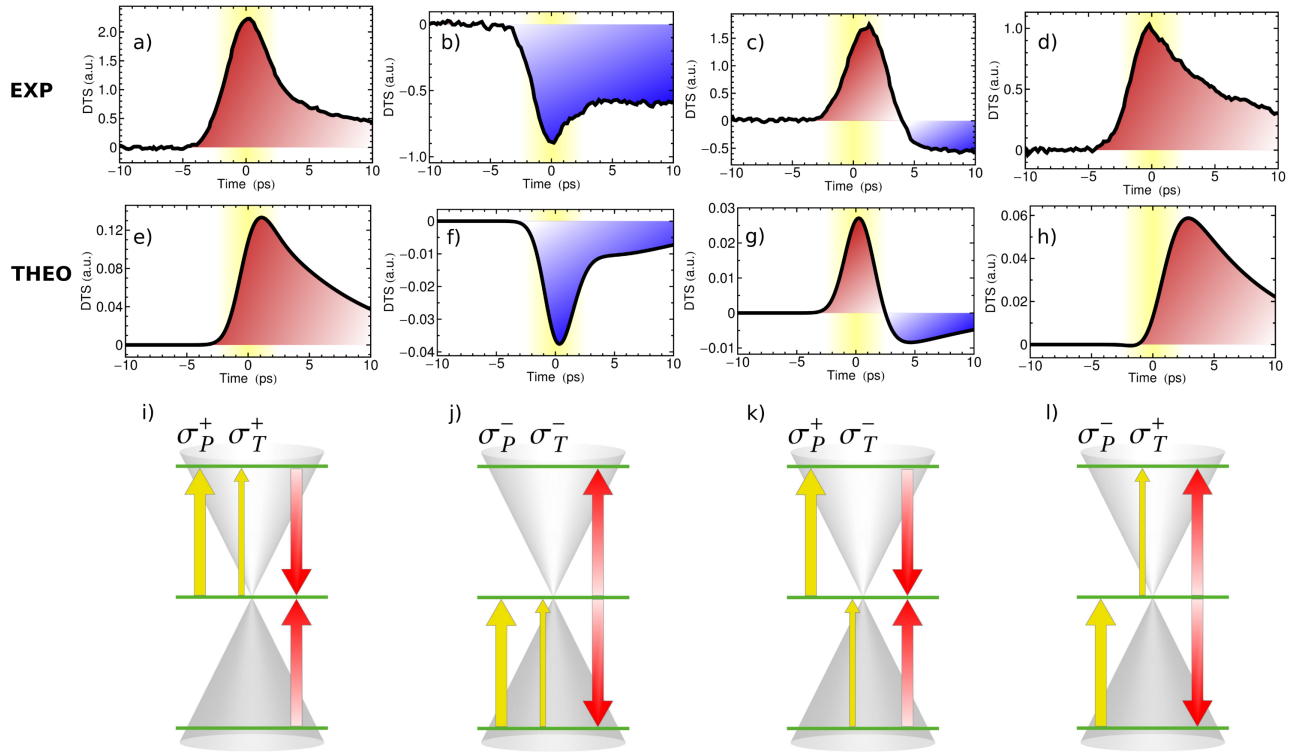
**Figure 9: Polarization-resolved differential transmission.** Time dependent differential transmission spectra for the four possible cases of combining pump ($\sigma_P$) and probe (or test $\sigma_T$) pulse polarization in experiment (upper panel (a)-(d)) and theory (middle panel (e)-(h)). The yellow shaded areas in the background illustrate the width of the pump pulse. The lower panel ((i)-(l)) shows the corresponding sketches illustrating the pump (thick yellow arrows) and probe (thin yellow arrows) pulses, as well as the Auger scattering channels (red arrows).

namics on femto- to picosecond timescales, the radiative decay is negligibly small in Landau-quantized graphene.

## 3.1 Carrier–carrier scattering

Carrier–carrier scattering mediated by the Coulomb interaction is known to be one of the most important scattering channels in semiconductors. In this section, its impact on the carrier dynamics in Landau-quantized graphene is investigated. In graphene the linear dispersion enables efficient Auger scattering, which is a scattering process characterized by one carrier changing the band while the other carrier remains in its initial band. The first experiment measuring the carrier dynamics in Landau-quantized graphene was performed by Plochocka et al. in 2009 [66]. Investigating rather high-energetic Landau levels ($n \sim 100$), they found a suppression of Auger processes as a consequence of the non-equidistant level spacings suggesting an overall suppression of Auger processes in Landau-quantized graphene [66].

Recently, the impact of Auger scattering to the low-energetic Landau levels was addressed in a joint experiment-theory study [70] combining microscopic modeling with polarization-resolved pump-probe experiments that have been performed by M. Mittendorff, S. Winnerl, and M. Helm at the Helmholtz–Zentrum Dresden–Rossendorf. The possibility to measure the differential transmission of selected Landau level transitions arises due to the non-equidistant Landau level spectrum and the optical selection rules dictating $n \rightarrow n \pm 1$. Using an optical excitation with an energy matching the transition energy $\Delta\epsilon_{0,+1} = \Delta\epsilon_{-1,0}$, the two allowed transitions among the Landau levels $LL_{-1}$, $LL_0$ and $LL_{+1}$ can be selected via the rotational direction of circularly polarized radiation, cf. Fig. 8. This results in four possibilities to combine pump and probe pulse polarization, cf. Fig. 8. Considering only the optical excitation, one expects a positive differential transmission (DT) of the probe pulse if the same polarization is used for both pulses (pump and probe), since the excitation of charge carriers enhances the Pauli blocking in this case. Conversely, if an opposite polarization is used for the pump and probe pulses, the optical excitation results in a suppression of Pauli blocking for the probe pulse with the result of a reduced transmission, hence we expect a negative DT signal.
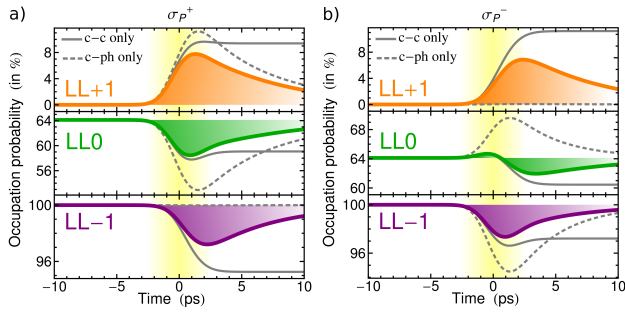
Figure 10: Landau level occupations for pumping with circularly polarized light. Temporal evolution of the three energetically lowest Landau levels after a $\sigma^+$ (a), and $\sigma^-$-polarized excitation (b).



Figure 11: Tuning the relative pumping strength with doping. In a system with a positive Fermi energy, the pumping with $\sigma^+$-polarized radiation is more efficient, since transitions induced by $\sigma^-$ light are strongly suppressed by Pauli blocking.

The upper panel of Fig. 9 illustrates the experimental results for the four configurations of pump and probe pulse polarizations at a magnetic field of $B$ = 4.2 T applying a pulse with a width of $\sigma_{FWHM}^{exp}$ = 2.7 ps and an energy of 75 meV. Comparing the experimental data with the expectation based on the occupation change induced by the optical excitation, a qualitative difference is observed in the case of pumping with $\sigma^-$-polarized radiation (Figs. 9(c), (d)): While the configuration $\sigma_P^-$, $\sigma_T^-$ ($\sigma^-$-polarized pump and test pulse) shows an initial increase (as expected) which is followed by an unexpected sign change to the negative region, the measured behavior in the configuration $\sigma_P^-$, $\sigma_T^+$ is completely contrary to what we would expect.

To explain these surprising experimental results, taking into consideration carrier–carrier scattering turns out to be of crucial importance. Moreover, to achieve an agreement between experiment and theory, a finite doping needs to be introduced to break the electron-hole symmetry. In an undoped system, the two configurations $\sigma_P^+$, $\sigma_T^+$ and $\sigma_P^-$, $\sigma_T^-$ (and likewise $\sigma_P^+$, $\sigma_T^-$ and $\sigma_P^-$, $\sigma_T^+$) would yield the exact same result. The assumption of a finite doping is further supported by experimental studies showing that multilayer epitaxial graphene samples grown on the C-terminated face of SiC (such a sample is used in the experiment) have a finite n-doping due to a charge transfer from the SiC substrate [124, 125]. Therefore, for the theoretical calculations a doping is assumed leading to an excess of electron concentration of $6 \times 10^{10}$ cm$^{-2}$ corresponding to a Fermi energy of $\epsilon_F$ = 28 meV. Using the Coulomb interaction determined within our microscopic approach (Eq. 29) including initial Landau level occupations corresponding to the assumed doping of the sample, the differential transmission is calculated, cf. middle panel of Fig. 9. To this end, the dynamics of the occupations is calculated using Eqs. (50),(51) and (53), (54). Then, the differential transmission is obtained exploiting the relation
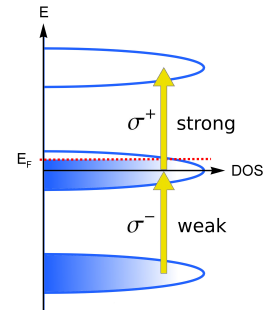
DTS$_{if}$ $\propto$ ($\Delta\rho_f - \Delta\rho_i$) [126], where $i$ and $f$ denote the initial and final states of the probed transition, and $\Delta\rho$ is the occupation change induced by the pump pulse and all scattering channels that are activated by it. This yields a good agreement with the measured results, cf. upper and middle panel of Fig. 9, providing valuable insights into the underlying carrier dynamics.

The theoretical calculations give access to the temporal evolutions of the involved Landau level occupations $\rho_{+1}$, $\rho_0$ and $\rho_{-1}$ after the application of a $\sigma^\pm$-polarized pump pulse, cf. Fig. 10, allowing us to explain the unexpected behavior in DT spectra. To identify the role of different scattering channels, they are separately switched on and off, cf. the solid gray line illustrating the dynamics due to carrier–carrier scattering only, and the dashed gray line indicating the phonon-induced dynamics. Note that the phonon-induced relaxation rates following from the microscopic description of the carrier–phonon scattering are not sufficiently strong to account for the fast decay rates observed in the experiment. However, the focus here lies in understanding the dynamics in the first few picoseconds after the optical excitation. Therefore, the carrier–phonon scattering is increased in order to match the experimentally observed decay rates at long times. Note that this fit does not change the dominant role of the Auger processes in the first ps.

Pumping with $\sigma^+$-polarized radiation, the transition LL$_0$ → LL$_{+1}$ is optically addressed which is reflected by a depopulation of LL$_0$, while LL$_{+1}$ is populated, cf. Fig. 10a. At the same time, $\rho_{-1}$ decreases which can unambiguously be attributed to inward Auger scattering involving the transitions LL$_{-1}$ → LL$_0$ and LL$_{+1}$ → LL$_0$, since this feature is not present in the dynamics without carrier–carrier scattering. The more interesting case is shown in Fig. 10b, where a $\sigma^-$-polarized excitation pulse is modeled. Although this optically induces the transition LL$_{-1}$ → LL$_0$,

the occupation $\rho_0$ shows only a minor increase in the beginning, then it starts to decrease already before the center of the pulse is reached. This means that although we optically pump carriers into the zeroth Landau level, its populations decreases. This surprising result can be explained by extremely efficient Auger scattering, which induces the transitions $LL_0 \rightarrow LL_{-1}$ and $LL_0 \rightarrow LL_{+1}$, thereby resulting in a quick depopulation of $\rho_0$. The crucial role of the Auger scattering becomes apparent by comparing the temporal evolution of $\rho_0$ to the case without Coulomb scattering (cf. dashed gray lines in Fig. 10b). Here, as expected, the population of the zeroth Landau level only increases during the entire time of the optical excitation.

To shed further light on the qualitatively different behavior when pumping with $\sigma^-$ and $\sigma^+$-polarized excitation, the relative excitation strengths between both cases is examined. Fig. 11 illustrates, how doping influences the pumping strength of the two optically allowed transitions in terms of Pauli blocking. Assuming a positive Fermi energy, pumping the transition $LL_0 \rightarrow LL_{+1}$ ($\sigma^+$) is more efficient, since the transition $LL_{-1} \rightarrow LL_0$ induced by $\sigma^-$ light is strongly suppressed by Pauli blocking. This explains the higher impact of Auger scattering when a $\sigma^-$-polarized excitation is applied resulting in the theoretically predicted and experimentally observed unexpected behavior in differential transmission spectra [70].

To sum up, sophisticated polarization-dependent pump-probe spectroscopy and microscopic modeling provide proof for efficient Auger scattering among the lowest Landau levels of graphene. The unexpected sign measured in polarization-resolved differential transmission spectra emerges since Auger scattering depopulates the zeroth Landau level faster than it is filled by optical excitation. This surprising effect appears, when the pumping efficiency is decreased due to an enhanced Pauli blocking as a result of a finite doping.

## 3.2 Carrier–phonon scattering

In this section, the impact of carrier-phonon scattering on the relaxation dynamics of Landau-quantized graphene is addressed. To this end, focusing on the three energetically lowest Landau levels, the dynamics of photo-excited charge carriers is investigated. Using a linear polarized excitation pulse of width $\sigma_{\text{FWHM}}^{\text{exp}} = 1.8\,\text{ps}$, and pump fluence $\epsilon_{\text{pf}} = 1\,\mu\text{Jcm}^{-2}$, the phonon-induced relaxation to equilibrium is examined, cf. Fig. 12. First, we discuss the impact of acoustic phonons, before the dynamics due to the optical phonon modes is analyzed in more detail.
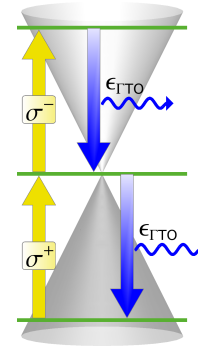


**Figure 12: Phonon-induced carrier relaxation.** Sketch of the energetically lowest Landau levels with the Dirac cone for vanishing magnetic fields in the background. The yellow arrows represent the linearly polarized optical excitation, which effectively pumps carriers from $LL_{-1}$ to $LL_{+1}$ in an undoped system. The phonon-induced inter-Landau level transitions, which are accompanied by the emission of phonons with the energy $\epsilon_{\Gamma\text{TO}}$, are indicated by the blue arrows.

### 3.2.1 Acoustic phonons

Since the momentum is not a good quantum number in Landau-quantized graphene, the phase space for phonon scattering is not restricted by momentum conservation. However, the carrier-phonon matrix element contains a Gaussian factor $e^{-l_B^2 q^2/2}$ (cf. Sect. 2.2.5) that limits the available phonon phase space to small $q$, thereby also restricting the maximal accessible phonon energy $\epsilon_{\text{ac}} = \hbar v_{\text{ac}} |\mathbf{q}|$. Therefore, acoustic phonon scattering is negligible for

$$\frac{l_B^2 q^2}{2} \gg 1. \tag{67}$$

Setting the phonon energy equal to the energy of an inter-Landau level transition $\Delta \epsilon_{if} = \epsilon_f - \epsilon_i$ up to a detuning given by the impurity induced Landau level broadening $\Gamma_{if} = \hbar \gamma_{if}^{\text{imp}}$, that is, $\epsilon_{\text{ac}} = \Delta \epsilon_{if} - \Gamma_{if}$, the phonon momentum $q$ is obtained and can be plugged into Eq. (67). This yields

$$\alpha_{i,f} = \left(\frac{v_F}{v_{\text{ac}}}\right)^2 \left(\lambda_f \sqrt{n_f} - \lambda_i \sqrt{n_i} - 1/\sqrt{2A_{\text{imp}}}\right)^2 \gg 1, \tag{68}$$

which does not depend on the magnetic field, but is solely determined by the transition under investigation and the parameter describing the impurity concentration $A_{\text{imp}}$. Since the velocity of acoustic phonons is much smaller than the Fermi velocity (by a factor of $\sim 10^{-2}$), the factor $(v_F/v_{\text{ac}})^2$ is large. For impurity-induced broadenings of 4 meV, 7 meV and 10 meV, the minimum of $\alpha_{n,n+1}$ is illustrated in Fig. 13. Here, we focus on intraband transitions between neighboring Landau levels $LL_n \rightarrow LL_{n+1}$, since
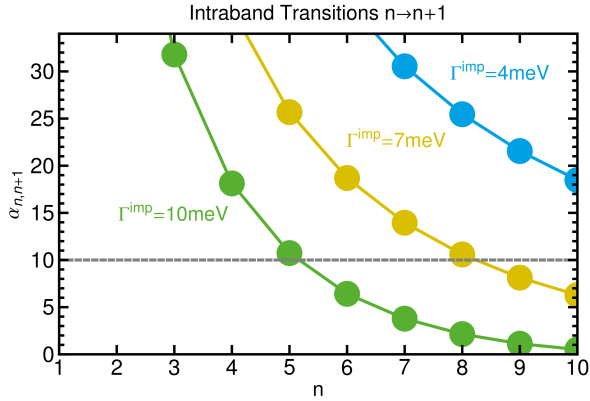
**Figure 13: Importance of acoustic phonons.** Minimal value of $\alpha_{n,n+1}$ defined in Eq. (68) is shown for the transition $LL_n \rightarrow LL_{n+1}$ as a function of $n$. Three different values (4meV, 7meV and 10meV) are used for the impurity-induced Landau level broadening. Assuming that $\alpha_{n,n+1} \approx 10$ fulfills the condition in Eq. (68), acoustic phonons are only important for transitions involving Landau levels higher than $n = 5$, cf. the dashed horizontal line.



**Figure 14: Carrier–optical–phonon relaxation rate.** Surface plot showing the carrier–phonon scattering rate involving $\Gamma$TO phonons inducing transitions $LL_{+1} \rightarrow LL_0$ and $LL_0 \rightarrow LL_{-1}$ as a function of time and magnetic field.

their transition energy is minimal. Furthermore, we take into account the $\Gamma$LA-mode, since its velocity $v_{ac}$ is larger compared to the $\Gamma$TA-mode [97]. We find that scattering with acoustic phonons is very small within the energetically lowest Landau levels up to $n = 5$ for broadenings not larger than 10meV, cf. 13. Consequently, the influence of acoustic phonons is neglected in the remainder of this work.

### 3.2.2 Optical phonons

The energy of optical phonons at the relevant high-symmetry points in the Brillouin zone of graphene is constant in good approximation, cf. Fig. 3. Therefore, phonon-induced transitions between Landau levels are strongly suppressed unless the respective transition is in resonance with the phonon energy. Since the transition energy depends on the magnetic field strength, cf. Eq. (12), the value of the magnetic field has a strong impact on the efficiency of carrier–phonon scattering. To study the magnetic field dependence of phonon-induced relaxation, the carrier dynamics is investigated for the exemplary $\Gamma$TO-mode [71, 72]. Considering only a single optical mode has the advantage of allowing an easier interpretation of the results. The gained insights can be readily generalized to other modes.

Solving the Bloch equations (50), (51) and (53),(54) , the temporal evolution of the polarizations $p_{if}$ and the occupations $\rho_i$ is obtained. Furthermore, we have access to the corresponding carrier–phonon relaxation rate $\gamma_\mu(t) =$
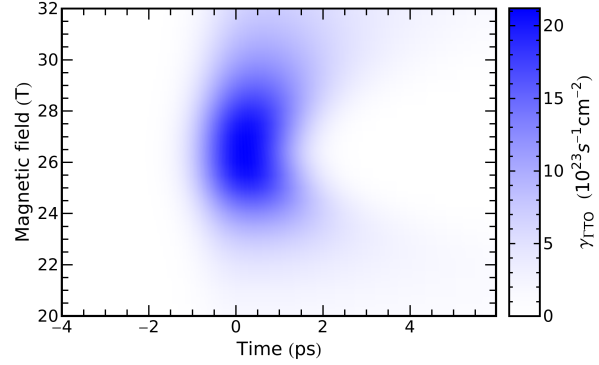
$1/A \sum_i \left( \dot{\rho}_i(t)|_\mu^{\mathrm{em}} - \dot{\rho}_i(t)|_\mu^{\mathrm{ab}} \right)$ that is defined as the occupation change due to the emission and absorption of phonons. It reflects the interaction strength of the mode $\mu$ and is explicitly calculated in every time step during and after the optical excitation. The temporal evolution of $\gamma_{\Gamma TO}(t)$ incorporating the transitions $LL_{+1} \rightarrow LL_0$ and $LL_0 \rightarrow LL_{-1}$ (cf. Fig. 12) is shown in Fig. 14 and illustrates a pronounced peak at a magnetic field of $B = 26.4$ T. This value corresponds to an inter-Landau level spacing between $LL_{\pm 1}$ and $LL_0$ matching the optical phonon energy. At different values of the magnetic field the energetic distance of the Landau levels changes and is detuned away from the resonance, consequently, the scattering rate decreases. The temporal decay of the scattering rate after the initial increase during the excitation is faster at the resonant magnetic field, which reflects the efficient phonon-induced equilibration of the system in this case. Considering transitions between other Landau levels, the resonance condition is met at different values of the magnetic field, including the experimentally more realistic regime of values of the order of 1 T.

The carrier–phonon scattering is very sensitive to the temperature that directly influences the phonon occupation $n_{\mathbf{p}\mu}$ given by a Bose–Einstein distribution. Therefore, the scattering rates $S_j^{\mathrm{in/out}}(t)|_{\mathrm{phon}}$ (cf. Eq. (56)) as well as the relaxation rate $\gamma_\mu(t)$ strongly depend on temperature. While phonon emission scales with $(n_{\mathbf{p}\mu} + 1)$ and is always possible provided that it is not forbidden by Pauli blocking, the absorption rates obey a $n_{\mathbf{p}\mu}$ dependence and are therefore strongly suppressed at small temperatures ($\lesssim 200$ K). Both emission and absorption rates increase with the temperature, whereas the overall relaxation rate (emission minus absorption) decreases, cf. Fig. 15. This is caused by Pauli blocking favoring the phonon absorption,
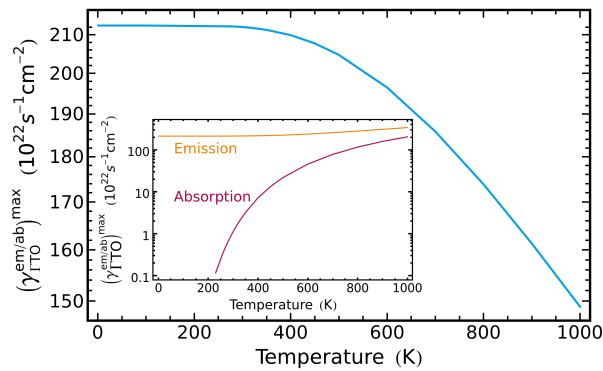
**Figure 15: Temperature dependence of the phonon-induced relaxation.** Dependence of the maximal carrier–phonon relaxation rate on temperature. The inset shows the contributions stemming from the emission and absorption of phonons separately. The Figure is taken from Ref. [72] Copyright (2014) by John Wiley & Sons.

at least in a weakly excited system without a population inversion. At low temperatures the phonon occupation $n_{\mathbf{p}\mu}$ is negligible compared to $(n_{\mathbf{p}\mu} + 1)$. As $n_{\mathbf{p}\mu}$ increases with the temperature, the prefactors for the emission $(n_{\mathbf{p}\mu} + 1)$ and absorption $n_{\mathbf{p}\mu}$ of phonons become comparable and similar to 1, and the Landau level occupations determine the respective scattering rates. The interplay between electron and phonon occupations results in an equilibration of the electronic system with the lattice, and to the emergence of the equilibrium Fermi–Dirac and Bose–Einstein distributions, respectively.

There are also recent studies investigating the phonon-induced relaxation rates exploiting Fermi's golden rule as well as the Huang–Rhys's lattice relaxation model [68, 69, 127]. Li and co-workers considered two-phonon scattering processes to bridge the inter-Landau level gap observing very slow relaxation times on the nanosecond time scale [127]. In their approach, besides the considered optical phonon, an additional acoustic phonon is introduced to ensure energy conservation. Taking into account the coupling of electrons to remote substrate phonons [128, 129], in Ref. [69] Wang et al. considered graphene on different polar substrates, which enables two-phonon scattering involving an acoustic and a polar surface optical phonon. This reveals relaxation rates that can reach the picosecond regime.

To sum up, carrier–phonon coupling can be drastically enhanced by tuning the magnetic field towards a resonance between the inter-Landau level energy and the optical phonon energy, giving rise to relaxation times on a picosecond time scale. The impact of acoustic phonon scattering on the carrier dynamics is negligible for low-energetic Landau levels unless the level broadening be-

comes so high that the Landau levels are not well-separated anymore.

# 4 Application-relevant many-particle phenomena

This section deals with potential applications of Landau-quantized graphene, where a strong external magnetic field provides an experimental knob by means of which the properties of graphene can be tuned. An investigation of the carrier dynamics reveals that the magnetic field yields promising possibilities that could be useful for the design of new optoelectronic devices. However, to exploit the unique properties of Landau-quantized graphene, the remaining substantial challenge is to implement magnetic fields into real devices. This could be, for example, achieved by growing graphene on ferromagnetic substrates or to use strain engineering to induce gauge fields that create pseudo-magnetic fields [130, 131].

Having established that Auger scattering is efficient between certain Landau levels of graphene in Section 3.1, it shall now be shown that this opens up the possibility to achieve a significant carrier multiplication (CM) [73]. This process, which is also referred to as multi exciton generation, is characterized by an increased number of excited charge carriers (electron-hole pairs) due to Auger scattering bridging the valence and conduction bands. The prediction of carrier multiplication for semiconductor quantum dots in 2002 [45] and its experimental verification two years later [132] has attracted much attention [133–138] and the concept has since been extended to other materials [41, 43, 44, 73, 139–143]. Its high relevance stems from the fact that it holds the potential to increase the power conversion efficiency of single-junction solar cells [144] above the Shockley–Queisser limit [145]. Moreover, carrier multiplication enables a fast detection of photons with a high responsivity. In graphene, the occurrence of carrier multiplication was theoretically predicted [41, 42] and experimentally confirmed [43, 44]. However, to exploit this effect for designing graphene-based photovoltaic devices, the challenge of charge carrier extraction in gapless systems needs to be solved. Here, a strategy to circumvent this problem is proposed by applying an external magnetic field which leads to a Landau quantization. For reasons of simplicity, the following investigation does not take phonon-induced relaxation processes into account, since they are strongly suppressed for magnetic fields that do not produce resonances between electronic transitions and phonon energies, as discussed in Sec. 3.2.
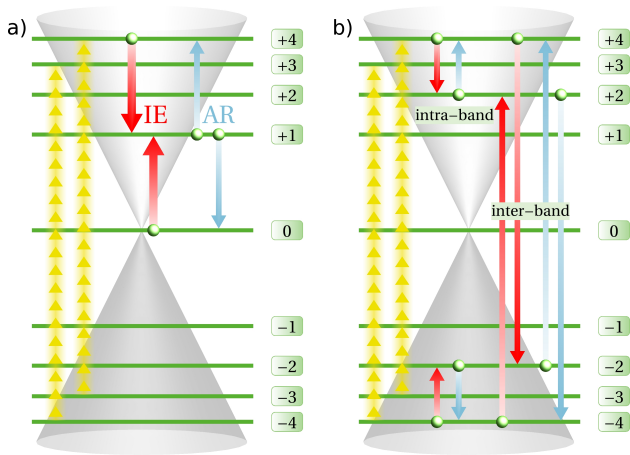
**Figure 16: Pumping scheme for carrier multiplication.** Two sketches of the low-energetic Landau levels in graphene with the Dirac cone in the background, where the yellow arrows indicate the optical excitation with linear polarized light inducing the transitions $LL_{\mp 4} \rightleftarrows LL_{\pm 3}$. (a) Carriers excited to $LL_{+4}$ can participate in a process called impact excitation (IE) which dominates against its inverse process called Auger recombination (AR). This leads to the excitation of an additional carrier from $LL_0$ to $LL_{+1}$. (b) Intra- and interband scattering channels between electrons that do not affect an occupation change, since they occur with the same probability as their respective inverse processes (cf. the red and blue arrows).



**Figure 17: Importance of Auger scattering.** Temporal evolution of the occupations $\rho_{+4}$ and $\rho_{+1}$ during an optical excitation as sketched in Fig. 16a. The dashed lines represent the dynamics in the absence of Auger scattering. The yellow region illustrates the width of the pump pulse ($\sigma_{FWHM}^{exp} = 1$ ps). The Figure is taken from Ref. [73] Copyright (2014) by Nature Publishing Group.

The suggested pumping scheme to achieve carrier multiplication is sketched in Fig. 16a. The strategy is to excite charge carriers to $LL_{+4}$, which induces an energy conserving scattering process including the transitions $LL_{+4} \rightarrow LL_{+1}$ and $LL_0 \rightarrow LL_{+1}$. This process is denoted as impact excitation (IE), since it effects the excitation of an additional charge carrier. Due to Pauli blocking, the inverse process which is termed Auger recombination (AR) is suppressed. Both IE and AR are Auger processes bridging the valence and conduction bands. As a consequence of the electron-hole symmetry, the discussed electronic transitions in the conduction band can also occur for holes in the valence band. Here, the pump pulse excites holes to $LL_{-4}$, and impact excitation induces the transitions $LL_{-4} \rightarrow LL_{-1}$ and $LL_0 \rightarrow LL_{-1}$ for holes (not shown). Staying in the electron picture, the transitions for holes must be inverted and correspond to the electronic transitions $LL_{-1} \rightarrow LL_{-4}$ and $LL_{-1} \rightarrow LL_0$. Therefore, in the pumping scheme illustrated in Fig. 16a, effectively the electronic transitions $LL_{+4} \rightarrow LL_{+1}$, $LL_{-1} \rightarrow LL_{-4}$, and $LL_{-1} \rightarrow LL_{+1}$ are induced by Auger scattering. This implies that the occupation of the zeroth Landau level does not change and its particular status as belonging to both bands does not need to be further investigated.

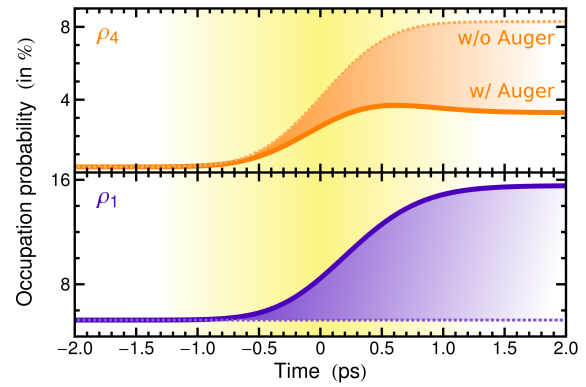Another consequence of the electron-hole symmetry is the suppression of other Coulomb-induced scattering channels within the energetically lowest Landau levels. Fig. 16b illustrates that intra- and interband scattering does not affect the Landau level occupations in an undoped graphene sample. The optical excitation creates an excess of electrons in $LL_{+4}$, while a lack of electrons is induced in $LL_{-4}$. Therefore, transitions that transfer electrons out of $LL_{+4}$ (cf. red arrows in Fig. 16b), and those that transfer them into $LL_{-4}$ (cf. blue arrows in Fig. 16b) are favored. Consequently, their contributions cancel out and carrier–carrier scattering other than Auger-type processes is suppressed.

The carrier dynamics is illustrated in Fig. 17 showing the occupations of $LL_{+4}$ and $LL_{+1}$ during a pulsed optical excitation of width $\sigma_{FWHM}^{exp} = 1$ ps, pump fluence $\epsilon_{pf} = 10^{-2}$ µJcm$^{-2}$, and an energy matching the transitions $LL_{\mp 4} \rightleftarrows LL_{\pm 3}$ which is $\epsilon_{+4} - \epsilon_{-3} \approx 280$ meV for a magnetic field of $B = 4$ T. The system is considered to be at room temperature and an impurity-induced Landau level broadening of $\Gamma^{imp} = 7$ meV is assumed. The dashed lines in Fig. 17 represent the dynamics without Auger scattering. In this case, the occupation $\rho_{+4}$ simply increases during the optical excitation, while $\rho_{+1}$ stays constant. Switching on Auger processes results in a transfer of occupation from $LL_{+4}$ to $LL_{+1}$, cf. the difference between dashed and solid lines in Fig. 17. However, the total increase of $\rho_{+1}$ (about 10%) exceeds the decrease of $\rho_{+4}$ (about 5%) by a factor of 2. This agrees with the simple picture sketched in Fig. 16a and is explained by a predominant impact excitation inducing the transitions $LL_{+4} \rightarrow LL_{+1}$ and $LL_0 \rightarrow LL_{+1}$.

The magnitude of the carrier multiplication is defined by the ratio between the carrier density change including all scattering channels and the purely pump-induced
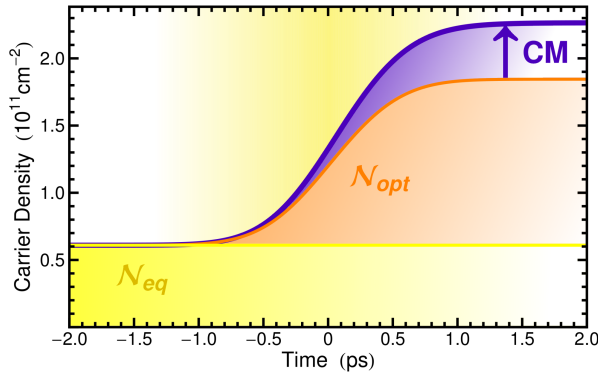
**Figure 18: Carrier multiplication.** Temporal evolution of the carrier density including the optical excitation as well as Coulomb scattering $\mathcal{N}$ (purple line), the carrier density in the absence of Coulomb scattering $\mathcal{N}_{opt}$ (orange line), and the constant equilibrium carrier density $\mathcal{N}_{eq}$ (yellow line) for the excitation scheme sketched in Fig. 16a. The yellow region in the backgrounds illustrates the optical excitation. Efficient Auger scattering leads to a carrier multiplication (CM) of approximately 1.3. The Figure is taken from Ref. [73] Copyright (2014) by Nature Publishing Group.

change of the carrier density:

$$\text{CM} = \frac{\mathcal{N} - \mathcal{N}_{eq}}{\mathcal{N}_{opt} - \mathcal{N}_{eq}}. \tag{69}$$

Here, $\mathcal{N}$ is the carrier density and $\mathcal{N}_{eq}$ its equilibrium value which corresponds to the thermal carrier distribution at a given temperature, while $\mathcal{N}_{opt}$ is the optically induced carrier density (in the absence of Coulomb scattering). To determine the value of CM, the temporal evolution of the carrier density is evaluated from the dynamics of the occupations according to the simple definition $\mathcal{N} = 4e_0 B/(\pi \hbar) \sum_{n \geq 1} \rho_n$ that is valid in an electron-hole symmetric system. The result is shown in Fig. 18 and illustrates an increase of the carrier density due to Auger scattering in particular reflecting the importance of the impact excitation (cf. Fig. 16a). The value of the carrier multiplication after an optical excitation with a pump fluence $\epsilon_{pf} = 10^{-2}$ μJcm$^{-2}$, an excitation energy of 280 meV, and a pulse width $\sigma_{\text{FWHM}}^{\exp} = 1$ ps is found to be CM ≈ 1.3.

Note that the maximal CM that can be achieved within the pumping scheme proposed in Fig. 16a is CM = 1.5. This becomes apparent in a simple example: Considering one excited electron per pumped transition (LL$_{-3}$ → LL$_{+4}$ and LL$_{-4}$ → LL$_{+3}$), there are four photo-excited charge carriers in the system (two electrons and holes, respectively). Then, one impact excitation process per band takes place generating in total two more charge carriers (an electron in LL$_{+1}$ and a hole in LL$_{-1}$). Dividing the total number of charge carriers after IE has taken place by the number of optically excited charge carriers yields the maximal possible value of CM = 6/4 = 1.5. It is achieved, if all photo-

excited charge carriers are involved in an impact excitation process. However, an optical excitation into a higher energetic Landau level is conceivable and is expected to induce higher values of the CM. In general, a low pump fluence is advantageous for CM, since a stronger optical excitation results in an increased asymmetry between the competing IE and AR scattering channels, leading to a faster equilibration of the corresponding scattering rates and reducing the time frame in which IE generates additional charge carriers. Moreover, changes of the initial occupations result in an increasing CM with lower temperatures and higher magnetic fields. Additionally, the CM increases with the magnetic field, as the effective pumping strength is reduced, cf. Eq. 64. Finally, a higher value of the CM is obtained for larger Landau level broadenings. The prediction of carrier multiplication in Landau-quantized graphene presented in this section suggests the design of graphene-based optoelectronic devices, such as photodetectors or even solar cells.

Besides the carrier multiplication, another technologically relevant process could be principally observed in Landau-quantized graphene: the appearance of population inversion suggesting the design of extremely tunable Landau level lasers. The idea of a two-dimensional (2D) Landau level laser dates back to 1986, when H. Aoki pointed out that the energy quantization in 2D semiconductor heterostructures can be utilized to tune the laser frequency and proposed a scheme to create population inversion (PI) in a junction heterostructure [146]. However, in conventional semiconductors the equidistant ladder of Landau levels and the optical selection rules coupling neighboring Landau levels make lasing difficult, since incoming radiation can not only stimulate the emission of photons (inducing an electronic transition to a lower Landau level), but can also be absorbed (inducing an electronic transition to a higher Landau level). This is not the case in graphene, where the linear bandstructure gives rise to a non-equidistant ladder of Landau levels and very specific selection rules in a magnetic field. Therefore, graphene provides better conditions for a Landau level laser, as was pointed out by Morimoto and coworkers [147].

One can think of generating a population inversion e.g. between LL$_{+2}$ and LL$_{+1}$ by strongly optically pumping carriers from LL$_{-3}$ to LL$_{+2}$. Based on the specific optical selection rules and the non-equidistant Landau-level spacing, we can selectively pump carriers into a single Landau level. Due to the strongly suppressed carrier–phonon scattering, an accumulation of carriers can be achieved in LL$_{+2}$ compared to the LL$_{+1}$ that remains unpopulated in undoped graphene samples [74]. Furthermore, a more sophisticated scheme has been suggested to create a popu-

lation inversion based on Auger scattering [74], which is remarkable, since Auger processes were shown to reduce the population inversion in graphene without a magnetic field [34], and have been considered the main obstacle for a graphene-based Landau level laser [66, 148]. The occurrence of a population inversion in this system would suggest the design of graphene-based Landau level lasers that are tunable over a large frequency range via the external magnetic field.

# 5 Conclusions

This work provides a review of very recent studies addressing the ultrafast carrier dynamics in Landau-quantized graphene. The focus lies on providing a microscopic view on elementary Coulomb- and phonon-induced scattering processes characterizing the non equilibrium inter-Landau level dynamics. The theoretical approach is based on the density matrix formalism including an impurity-induced Landau level broadening as well as carrier–light, carrier–carrier, and carrier–phonon scattering channels that dominate the carrier dynamics occurring on femto-to picosecond time scales. Semiconductor Bloch equations are derived for Landau-quantized graphene providing microscopic access to time-resolved dynamics of optically excited carriers between the Landau levels.

Auger processes have been identified as the crucial scattering channel acting on a femtosecond timescale. This is a surprising finding considering the non-equidistant Landau quantization in graphene. However, due to the square-root dependence of the energy on the Landau level index, one can always find transitions that fulfill the conservation of energy opening up the channel for Auger scattering. A recent joint experiment-theory study nicely demonstrates the crucial role of Auger processes by investigating time-resolved and polarization-dependent differential transmission spectra. Efficient Auger processes are shown to even dominate the carrier dynamics during the optical excitation giving rise to an ultrafast depopulation of optically pumped Landau levels. Furthermore, in a recent study, the occurrence of a significant Auger-induced carrier multiplication has been theoretically predicted suggesting the application of graphene in highly efficient optoelectronic devices. The experimental demonstration of this technologically highly relevant effect is still on the agenda of current research. Finally, we discuss the possibility to achieve a population inversion among Landau levels presenting the crucial prerequisite for the design of extremely tunable Landau level lasers.

In summary, the field investigating the carrier dynamics in Landau-quantized graphene is of huge interest both for fundamental as well as application-oriented research. Many interesting ultrafast phenomena still remain to be explored.

# References

[1] F. Bonaccorso, Z. Sun, T. Hasan, and A. C. Ferrari. Graphene photonics and optoelectronics. *Nature Photon.*, 4:611–622, 2010.

[2] A. K. Geim and K. S. Novoselov. The rise of graphene. *Nat. Mater.*, 6(3):183–191, 2007.

[3] A. K. Geim. Graphene: Status and Prospects. *Science*, 324:1530–1534, 2009.

[4] P. Avouris and C. Dimitrakopoulos. Graphene: synthesis and applications. *Mater. Today*, 15(3):86 – 97, 2012.

[5] A.J. Van Bommel, J.E. Crombeen, and A. Van Tooren. LEED and Auger electron observations of the SiC(0001) surface. *Surf. Sci.*, 48:463–472, 1975.

[6] K. S. Novoselov, A. K. Geim, S. V. Morozov, D. Jiang, Y. Zhang, S. V. Dubonos, I. V. Grigorieva, and A. A. Firsov. Electric Field Effect in Atomically Thin Carbon Films. *Science*, 306:666–669, 2004.

[7] P. R. Wallace. The Band Theory of Graphite. *Phys. Rev.*, 71:622–634, May 1947.

[8] O. Klein. Die Reflexion von Elektronen an einem Potentialsprung nach der relativistischen Dynamik von Dirac. *Zeitschrift für Physik*, 53:157–165, 1929.

[9] M. I. Katsnelson, K. S. Novoselov, and A. K. Geim. Chiral tunnelling and the Klein paradox in graphene. *Nat. Phys.*, 2:620–625, 2006.

[10] F. Xia, T. Mueller, Y.-M. Lin, A. Valdes-Garcia, and P. Avouris. Ultrafast graphene photodetector. *Nature Nano.*, 4(12):839–843, 2009.

[11] T. Mueller, F. Xia, and P. Avouris. Graphene photodetectors for high-speed optical communications. *Nat. Photon.*, 4(5):297–301, May 2010.

[12] X. Gan, R.-J. Shiue, Y. Gao, I. Meric, T. F. Heinz, K. Shepard, J. Hone, S. Assefa, and D. Englund. Chip-integrated ultrafast graphene photodetector with high responsivity. *Nature Photon.*, 7(11):883–887, 2013.

[13] Q. Bao, H. Zhang, Y. Wang, Z. Ni, Y. Yan, Z. X. Shen, K. P. Loh, and D. Y. Tang. Layer Graphene as a Saturable Absorber for Ul-

trafast Pulsed Lasers. *Adv. Funct. Mater.*, 19:3077–3083, 2009.

[14] H. Zhang, Q. Bao, D. Tang, L. Zhao, and K. Loh. Large energy soliton erbium-doped fiber laser with a graphene-polymer composite mode locker. *Appl. Phys. Lett.*, 95(14):141103, 2009.

[15] Z. Sun, T. Hasan, F. Torrisi, D. Popa, G. Privitera, F. Wang, F. Bonaccorso, D. M. Basko, and A. C. Ferrari. Graphene Mode-Locked Ultrafast Laser. *ACS Nano*, 4(2):803–810, 2010.

[16] X. Wang, L. Zhi, and K. Müllen. Transparent, Conductive Graphene Electrodes for Dye-Sensitized Solar Cells. *Nano Lett.*, 8(1):323–327, 2008. PMID: 18069877.

[17] Z. Liu, Q. Liu, Y. Huang, Y. Ma, S. Yin, X. Zhang, W. Sun, and Y. Chen. Organic Photovoltaic Devices Based on a Novel Acceptor Material: Graphene. *Adv. Mat.*, 20(20):3924–3930, 2008.

[18] P. Matyba, H. Yamaguchi, G. Eda, M. Chhowalla, L. Edman, and N. D. Robinson. Graphene and Mobile Ions: The Key to All-Plastic, Solution-Processed Light-Emitting Devices. *ACS Nano*, 4(2):637–642, 2010. PMID: 20131906.

[19] S. Bae, H. Kim, Y. Lee, X. Xu, J.-S. Park, Y. Zheng, J. Balakrishnan, T. Lei, H. Ri Kim, Y. I. Song, Y.-J. Kim, K. S. Kim, B. Ozyilmaz, J.-H. Ahn, B. H. Hong, and S. Iijima. Roll-to-roll production of 30-inch graphene films for transparent electrodes. *Nat. Nano.*, 5(8):574–578, August 2010.

[20] T. Kampfrath, L. Perfetti, F. Schapper, C. Frischkorn, and M. Wolf. Strongly Coupled Optical Phonons in the Ultrafast Dynamics of the Electronic Energy and Current Relaxation in Graphite. *Phys. Rev. Lett.*, 95:187403, 2005.

[21] S. Butscher, F. Milde, M. Hirtschulz, E. Malić, and A. Knorr. Hot electron relaxation and phonon dynamics in graphene. *Appl. Phys. Lett.*, 91(20):203103, 2007.

[22] J. M. Dawlaty, S. Shivaraman, M. Chandrashekhar, F. Rana, and M. G. Spencer. Measurement of ultrafast carrier dynamics in epitaxial graphene. *Appl. Phys. Lett.*, 92:042116, 2008.

[23] D. Sun, Z.-K. Wu, C. Divin, X. Li, C. Berger, W. A. de Heer, P. N. First, and T. B. Norris. Ultrafast Relaxation of Excited Dirac Fermions in Epitaxial Graphene Using Optical Differential Transmission Spectroscopy. *Phys. Rev. Lett.*, 101:157402, 2008.

[24] F. Rana, P. A. George, J. H. Strait, J. Dawlaty, S. Shivaraman, M. Chandrashekhar, and M. G. Spencer. Carrier recombination and generation rates for intravalley and intervalley phonon scattering in graphene. *Phys. Rev. B*, 79:115447, 2009.

[25] S. Winnerl, M. Orlita, P. Plochocka, P. Kossacki, M. Potemski, T. Winzer, E. Malic, A. Knorr, M. Sprinkle, C. Berger, W. A. de Heer, H. Schneider, and M. Helm. Carrier Relaxation in Epitaxial Graphene Photoexcited Near the Dirac Point. *Phys. Rev. Lett.*, 107:237401, 2011.

[26] M. Breusing, S. Kuehn, T. Winzer, E. Malić, F. Milde, N. Severin, J. P. Rabe, C. Ropers, A. Knorr, and T. Elsaesser. Ultrafast nonequilibrium carrier dynamics in a single graphene layer. *Phys. Rev. B*, 83:153410, 2011.

[27] R. Kim, V. Perebeinos, and P. Avouris. Relaxation of optically excited carriers in graphene. *Phys. Rev. B*, 84:075449, 2011.

[28] T. Winzer, A. Knorr, M. Mittendorff, S. Winnerl, M.-B. Lien, D. Sun, T. B. Norris, M. Helm, and E. Malic. Absorption saturation in optically excited graphene. *Appl. Phys. Lett.*, 101(22):221115, 2012.

[29] E. Malic, T. Winzer, and A. Knorr. Efficient orientational carrier relaxation in optically excited graphene. *Appl. Phys. Lett.*, 101(21):213110, 2012.

[30] D. Sun, C. Divin, M. Mihnev, T. Winzer, E. Malic, A. Knorr, J. E. Sipe, C. Berger, W. A. de Heer, P. N. First, and T. B. Norris. Current relaxation due to hot carrier scattering in graphene. *New J. Phys.*, 14(10):105012, 2012.

[31] I. Gierz, J. C. Petersen, M. Mitrano, C. Cacho, I. C. E. Turcu, E. Springate, A. Stöhr, A. Köhler, U. Starke, and A. Cavalleri. Snapshots of non-equilibrium Dirac carrier distributions in graphene. *Nature Mater.*, 12(12):1119–1124, 2013.

[32] S. Winnerl, F. Göttfert, M. Mittendorff, H. Schneider, M. Helm, T. Winzer, E. Malic, A. Knorr, M. Orlita, M. Potemski, M. Sprinkle, C. Berger, and W. A. de Heer. Time-resolved spectroscopy on epitaxial graphene in the infrared spectral range: relaxation dynamics and saturation behavior. *J. Phys. Condens. Matter*, 25(5):054202, 2013.

[33] J. C. Johannsen, S. Ulstrup, F. Cilento, A. Crepaldi, M. Zacchigna, C. Cacho, I. C. E. Turcu, E. Springate, F. Fromm, C. Raidel, T. Seyller, F. Parmigiani, M. Grioni, and P. Hofmann. Direct View of Hot Carrier Dynamics in Graphene. *Phys. Rev. Lett.*, 111:027403, 2013.

[34] T. Winzer, E. Malić, and A. Knorr. Microscopic mechanism for transient population inversion and optical gain in graphene. *Phys. Rev. B*, 87:165413, 2013.

[35] F. Kadi, T. Winzer, E. Malic, A. Knorr, F. Göttfert, M. Mittendorff, S. Winnerl, and M. Helm. Microscopic Description of Intraband Absorption in Graphene: The Occurrence of Transient Negative Differential Transmission. *Phys. Rev. Lett.*, 113:035502, 2014.

[36] M. Mittendorff, T. Winzer, E. Malic, A. Knorr, C. Berger, W. A. de Heer, H. Schneider, M. Helm, and S. Winnerl. Anisotropy of Excitation and Relaxation of Photogenerated Charge Carriers in Graphene. *Nano Lett.*, 14(3):1504–1507, 2014.

[37] T. Winzer, R. Ciesielski, M. Handloser, A. Comin, A. Hartschuh, and E. Malic. Microscopic View on the Ultrafast Photoluminescence from Photoexcited Graphene. *Nano Lett.*, 15(2):1141–1145, 2015.

[38] E. Malic and A. Knorr. *Graphene and Carbon Nanotubes: Ultrafast Optics and Relaxation Dynamics*. Wiley-VCH, 2013.

[39] E. Malic, T. Winzer, E. Bobkin, and A. Knorr. Microscopic theory of absorption and ultrafast many-particle kinetics in graphene. *Phys. Rev. B*, 84:205406, 2011.

[40] F. Rana. Electron-hole generation and recombination rates for Coulomb scattering in graphene. *Phys. Rev. B*, 76:155431, 2007.

[41] T. Winzer, A. Knorr, and E. Malic. Carrier Multiplication in Graphene. *Nano Lett.*, 10:4839–4843, 2010.

[42] T. Winzer and E. Malic. Impact of Auger processes on carrier dynamics in graphene. *Phys. Rev. B*, 85:241404, 2012.

[43] D. Brida, A. Tomadin, C. Manzoni, Y. J. Kim, A. Lombardo, S. Milana, R. R. Nair, K. S. Novoselov, A. C. Ferrari, G. Cerullo, and M. Polini. Ultrafast collinear scattering and carrier multiplication in graphene. *Nature Commun.*, 4:1987, 2013.

[44] T. Plötzing, T. Winzer, E. Malic, D. Neumaier, A. Knorr, and H. Kurz. Experimental Verification of Carrier Multiplication in Graphene. *Nano Lett.*, 14(9):5371–5375, 2014. PMID: 25144320.

[45] A. J. Nozik. Quantum dot solar cells. *Physica E*, 14:115 – 120, 2002.

[46] V. Ryzhii, M. Ryzhii, and T. Otsuji. Negative dynamic conductivity of graphene with optical pumping. *J. Appl. Phys.*, 101:083114, 2007.

[47] T. Li, L. Luo, M. Hupalo, J. Zhang, M. C. Tringides, J. Schmalian, and J. Wang. Femtosecond Population Inversion and Stimulated Emission of Dense Dirac Fermions in Graphene. *Phys. Rev. Lett.*, 108:167401, 2012.

[48] S. Boubanga-Tombet, S. Chan, T. Watanabe, A. Satou, V. Ryzhii, and T. Otsuji. Ultrafast carrier dynamics and terahertz emission in optically pumped graphene at room temperature. *Phys. Rev. B*, 85:035443, 2012.

[49] R. Jago, T. Winzer, A. Knorr, and E. Malic. Graphene as gain medium for broadband lasers. *Phys. Rev. B*, 92:085407.

[50] F. D. M. Haldane. Model for a Quantum Hall Effect without Landau Levels: Condensed-Matter Realization of the "Parity Anomaly". *Phys. Rev. Lett.*, 61:2015–2018, 1988.

[51] M. L. Sadowski, G. Martinez, M. Potemski, C. Berger, and W. A. de Heer. Landau Level Spectroscopy of Ultrathin Graphite Layers. *Phys. Rev. Lett.*, 97:266405, 2006.

[52] P. Plochocka, C. Faugeras, M. Orlita, M. L. Sadowski, G. Martinez, M. Potemski, M. O. Goerbig, J.-N. Fuchs, C. Berger, and W. A. de Heer. High-Energy Limit of Massless Dirac Fermions in Multilayer Graphene using Magneto-Optical Transmission Spectroscopy. *Phys. Rev. Lett.*, 100:087401, 2008.

[53] M. Orlita, C. Faugeras, P. Plochocka, P. Neugebauer, G. Martinez, D. K. Maude, A.-L. Barra, M. Sprinkle, C. Berger, W. A. de Heer, and M. Potemski. Approaching the Dirac Point in High-Mobility Multilayer Epitaxial Graphene. *Phys. Rev. Lett.*, 101:267601, 2008.

[54] D. L. Miller, K. D. Kubista, G. M. Rutter, M. Ruan, W. A. de Heer, P. N. First, and J. A.A. Stroscio. Observing the Quantization of Zero Mass Carriers in Graphene. *Science*, 324:924–927, 2009.

[55] K. S. Novoselov, A. K. Geim, S. V. Morozov, D. Jiang, M. I. Katsnelson, I. V. Grigorieva, S. V. Dubonos, and A. A. Firsov. Two-dimensional gas of massless Dirac fermions in graphene. *Nature*, 438:197–200, 2005.

[56] Y. Zhang, Y.-W. Tan, H. L. Stormer, and P. Kim. Experimental observation of the quantum Hall effect and Berry's phase in graphene. *Nature*, 438:201–204, 2005.

[57] X. Du, I. Skachko, F. Duerr, A. Luican, and E. Y. Andrei. Fractional quantum Hall effect and insulating phase of Dirac electrons in graphene. *Nature*, 462:192–195, 2009.

[58] K. I. Bolotin, F. Ghahari, M. D. Shulman, H. L. Stormer, and P. Kim. Observation of the fractional quantum Hall effect in graphene. *Nature*, 462:196–199, 2009.

[59] L. A. Ponomarenko, R. V. Gorbachev, G. L. Yu, D. C. Elias, R. Jalil, A. A. Patel, A. Mishchenko, A. S. Mayorov, C. R. Woods, J. R. Wallbank, M. Mucha-Kruczynski, B. A. Piot, M. Potemski, I. V. Grigorieva, K. S. Novoselov, F. Guinea, V. I. Fal'ko, and A. K. Geim. Cloning of Dirac fermions in graphene superlattices. *Nature*, 497:594–597, 2013.

[60] C. R. Dean, L. Wang, P. Maher, C. Forsythe, F. Ghahari, Y. Gao, J. Katoch, M. Ishigami, P. Moon, M. Koshino, T. Taniguchi, K. Watanabe, K. L. Shepard, J. Hone, and P. Kim. Hofstadter's butterfly and the fractal quantum Hall effect in moire superlattices. *Nature*, 497:598–602, 2013.

[61] B. Hunt, J. D. Sanchez-Yamagishi, A. F. Young, M. Yankowitz, B. J. LeRoy, K. Watanabe, T. Taniguchi, P. Moon, M. Koshino, P. Jarillo-Herrero, and R. C. Ashoori. Massive Dirac Fermions and Hofstadter Butterfly in a van der Waals Heterostructure. *Science*, 340:1427–1430, 2013.

[62] I. Crassee, J. Levallois, A. L. Walter, M. Ostler, A. Bostwick, E. Rotenberg, T. Seyller, D. van der Marel, and A. B. Kuzmenko.

[63] Giant Faraday rotation in single- and multilayer graphene. *Nat. Phys.*, 7:48–51, 2011.

[63] C. Drexler, S. A. Tarasenko, P. Olbrich, J. Karch, M. Hirmer, F. Muller, M. Gmitra, J. Fabian, R. Yakimova, S. Lara-Avila, S. Kubatkin, M. Wang, R. Vajtai, P. M. Ajayan, J. Kono, and S. D. Ganichev. Magnetic quantum ratchet effect in graphene. *Nat. Nano.*, 8:104–107, 2013.

[64] Y. Kawano. Wide-band frequency-tunable terahertz and infrared detection with graphene. *Nanotechnol.*, 24:214004, 2013.

[65] M. O. Goerbig. Electronic properties of graphene in a strong magnetic field. *Rev. Mod. Phys.*, 83:1193–1243, 2011.

[66] P. Plochocka, P. Kossacki, A. Golnik, T. Kazimierczuk, C. Berger, W. A. de Heer, and M. Potemski. Slowing hot-carrier relaxation in graphene using a magnetic field. *Phys. Rev. B*, 80:245415, 2009.

[67] M. Mittendorff, M. Orlita, M. Potemski, C. Berger, W. A. de Heer, H. Schneider, M. Helm, and S. Winnerl. Intraband carrier dynamics in Landau-quantized multilayer epitaxial graphene. *New J. Phys.*, 16:123021, 2014.

[68] Z.-W. Wang, L. Liu, L. Shi, X.-J. Gong, W.-P. Li, and K. Xu. The Temperature Dependence of Optical Phonon Scattering in Graphene under Strong Magnetic Field. *J. Phys. Soc. Jpn.*, 82:094606, 2013.

[69] Z.-W. Wang, L. Liu, and Z.-Q. Li. Fast two-phonon relaxation process between the Landau levels of graphene on different polar substrates. *Europhys. Lett.*, 108:36005, 2014.

[70] M. Mittendorff, F. Wendler, E. Malic, A. Knorr, M. Orlita, M. Potemski, C. Berger, W. A. de Heer, H. Schneider, M. Helm, and S. Winnerl. Carrier dynamics in Landau-quantized graphene featuring strong Auger scattering. *Nature Phys.*, 11:75–81, 2015.

[71] F. Wendler, A. Knorr, and E. Malic. Resonant carrier–phonon scattering in graphene under Landau quantization. *Appl. Phys. Lett.*, 103(25):253117, 2013.

[72] F. Wendler and E. Malic. Carrier-phonon scattering in Landau-quantized graphene. *Phys. Status Solidi B*, 251:2541–2544, 2014.

[73] F. Wendler, A. Knorr, and E. Malic. Carrier multiplication in graphene under Landau quantization. *Nature Commun.*, 5:3703, 2014.

[74] F. Wendler and E. Malic. Towards a tunable graphene-based Landau level laser in the terahertz regime. *Sci. Rep.*, 5:12646, 2015.

[75] C. Cohen-Tannoudji, B. Diu, and F. Laloë. *Quantenmechanik: Band 1*. de Gryter, 2009.

[76] F. Bloch. Über die Quantenmechanik der Elektronen in Kristallgittern. *Zeitschrift für Physik*, 52(7-8):555–600, 1929.

[77] R. Peierls. Zur Theorie des Diamagnetismus von Leitungselektronen. *Zeitschrift fuer Physik*, 80(11-12):763–791, 1933.

[78] C. Strahberger. *Vertikaler Transport und extreme Magnetfelder in Halbleitern*. PhD thesis, Technischen Universitaet Muenchen, 2001.

[79] J. Zak. Magnetic Translation Group. *Phys. Rev.*, 134:A1602–A1606, 1964.

[80] J. Zak. Weyl-Heisenberg group and magnetic translations in finite phase space. *Phys. Rev. B*, 39:694–700, 1989.

[81] D. Yoshioka. *The Quantum Hall Effect*. Springer Berlin Heidelberg, 2002.

[82] M. Kohmoto, B. I. Halperin, and Y.-S. Wu. Quantized Hall effect in 3D periodic systems. *Physica B: Condensed Matter*, 184(1-4):30 – 33, 1993.

[83] D. R. Hofstadter. Energy levels and wave functions of Bloch electrons in rational and irrational magnetic fields. *Phys. Rev. B*, 14:2239–2249, Sep 1976.

[84] A. Trellakis. Nonperturbative Solution for Bloch Electrons in Constant Magnetic Fields. *Phys. Rev. Lett.*, 91:056405, Aug 2003.

[85] G. H. Wannier. A Result Not Dependent on Rationality for Bloch Electrons in a Magnetic Field. *Phys. Status Solidi B*, 88:757–765, 1978.

[86] G. H. Wannier. The Structure of Electronic Excitation Levels in Insulating Crystals. *Phys. Rev.*, 52:191–197, Aug 1937.

[87] J. Luttinger. The Effect of a Magnetic Field on Electrons in a Periodic Potential. *Phys. Rev.*, 84:814–817, Nov 1951.

[88] W. Kohn. Theory of Bloch Electrons in a Magnetic Field: The Effective Hamiltonian. *Phys. Rev.*, 115:1460, 1959.

[89] G. Gumbs, A. Iurov, D. Huang, and L. Zhemchuzhna. Revealing Hofstadter spectrum for graphene in a periodic potential. *Phys. Rev. B*, 89:241407, Jun 2014.

[90] S. Reich, J. Maultzsch, C. Thomsen, and P. Ordejón. Tight-binding description of graphene. *Phys. Rev. B*, 66:035412, Jul 2002.

[91] A. H. Castro Neto, F. Guinea, N. M. R. Peres, K. S. Novoselov, and A. K. Geim. The electronic properties of graphene. *Rev. Mod. Phys.*, 81:109–162, 2009.

[92] Y. Zhang, Z. Jiang, J. Small, M. Purewal, Y.-W. Tan, M. Fazlollahi, J. Chudow, J. Jaszczak, H. Stormer, and P. Kim. Landau-Level Splitting in Graphene in High Magnetic Fields. *Phys. Rev. Lett.*, 96:136806, Apr 2006.

[93] L. Onsager. Interpretation of the de Haas-van Alphen effect. *Philosophical Magazine Series 7*, 43(344):1006–1008, 1952.

[94] Y. Lozovik and A. Sokolik. Influence of Landau level mixing on the properties of elementary excitations in graphene in strong magnetic field. *Nanoscale Res. Lett.*, 7:134, 2012.

[95] M. Mohr, J. Maultzsch, E. Dobardžić, S. Reich, I. Milošević, M. Damnjanović, A. Bosak, M. Krisch, and C. Thomsen. Phonon dispersion of graphite by inelastic x-ray scattering. *Phys. Rev. B*, 76:035439, 2007.

[96] J. Maultzsch, S. Reich, C. Thomsen, H. Requardt, and P. Ordejón. Phonon Dispersion in Graphite. *Phys. Rev. Lett.*, 92:075501, Feb 2004.

[97] K. Michel and B. Verberck. Theory of the evolution of phonon spectra and elastic constants from graphene to graphite. *Phys. Rev. B*, 78:085424, Aug 2008.

[98] E. Akkermans and G. Montambaux. *Mesoscopic Physics of Electrons and Photons*. Cambridge University Press, 2007.

[99] K. M. Rao and J. E. Sipe. Coherent photocurrent control in graphene in a magnetic field. *Phys. Rev. B*, 86:115427, 2012.

[100] R. C. Jones. A New Calculus for the Treatment of Optical Systems. *J. Opt. Soc. Am.*, 31:488–493, 1941.

[101] A. Tomadin, D. Brida, G. Cerullo, A. C. Ferrari, and M. Polini. Nonequilibrium dynamics of photoexcited electrons in graphene: Collinear scattering, Auger processes, and the impact of screening. *Phys. Rev. B*, 88:035430, 2013.

[102] R. Roldan, J.-N. Fuchs, and M. Goerbig. Collective modes of doped graphene and a standard two-dimensional electron gas in a strong magnetic field: Linear magnetoplasmons versus magnetoexcitons. *Phys. Rev. B*, 80:085408, Aug 2009.

[103] R. Roldan, M. O. Goerbig, and J.-N. Fuchs. The magnetic field particle-hole excitation spectrum in doped graphene and in a standard two-dimensional electron gas. *Semicond. Sci. Technol.*, 25(3):034005, 2010.

[104] E. Mariani and F. von Oppen. Temperature-dependent resistivity of suspended graphene. *Phys. Rev. B*, 82:195403, 2010.

[105] H. Suzuura and T. Ando. Phonons and electron-phonon scattering in carbon nanotubes. *Phys. Rev. B*, 65:235412, 2002.

[106] T. Ando. Anomaly of Optical Phonon in Monolayer Graphene. *J. Phys. Soc. Jpn.*, 75:124701, 2006.

[107] C. L. Kane and E. J. Mele. Size, Shape, and Low Energy Electronic Structure of Carbon Nanotubes. *Phys. Rev. Lett.*, 78:1932–1935, 1997.

[108] W.-K. Tse and S. Das Sarma. Energy relaxation of hot Dirac fermions in graphene. *Phys. Rev. B*, 79:235406, Jun 2009.

[109] S. Piscanec, M. Lazzeri, F. Mauri, A. C. Ferrari, and J. Robertson. Kohn Anomalies and Electron-Phonon Interactions in Graphite. *Phys. Rev. Lett.*, 93:185503, 2004.

[110] W. Kohn. Image of the Fermi Surface in the Vibration Spectrum of a Metal. *Phys. Rev. Lett.*, 2:393–394, 1959.

[111] H. Haug and S. W. Koch. *Quantum Theory of the Optical and Electronic Properties of Semiconductors*. World Scientific, 2009.

[112] M. Kira and S.W. Koch. Many-body correlations and excitonic effects in semiconductor spectroscopy. *Prog. Quantum Electron.*, 30(5):155 – 296, 2006.

[113] T. Ando and Y. Uemura. Theory of Quantum Transport in a Two-Dimensional Electron System under Magnetic Fields. I. Characteristics of Level Broadening and Transport under Strong Fields. *J. Phys. Soc. Jpn.*, 36:959–967, 1974.

[114] E. Stock, M.-R. Dachner, T. Warming, A. Schliwa, A. Lochmann, A. Hoffmann, A. I. Toropov, A. K. Bakarov, I. A. Derebezov, M. Richter, V. A. Haisler, A. Knorr, and D. Bimberg. Acoustic and optical phonon scattering in a single In(Ga)As quantum dot. *Phys. Rev. B*, 83:041304, 2011.

[115] J. Förstner, C. Weber, J. Danckwerts, and A. Knorr. Phonon-induced damping of Rabi oscillations in semiconductor quantum dots. *Phys. Status Solidi B*, 238:419–422, 2003.

[116] N. H. Shon and T. Ando. Quantum Transport in Two-Dimensional Graphite System. *J. Phys. Soc. Jpn.*, 67(7):2421–2429, 1998.

[117] T. Dittrich, P. Haengi, G.-L. Ingold, B. Kramer, G. Schoen, and W. Zwerger. *Quantum Transport and Dissipation*. Wiley-VCH, 1998.

[118] J. Martin, N. Akerman, G. Ulbricht, T. Lohmann, J. H. Smet, K. von Klitzing, and A. Yacoby. Observation of electron-hole puddles in graphene using a scanning single-electron transistor. *Nat. Phys.*, 4(2):144–148, February 2008.

[119] Y. Zhang, V. W. Brar, C. Girit, A. Zettl, and Michael F. Crommie. Origin of spatial charge inhomogeneity in graphene. *Nat. Phys.*, 5(10):722–726, October 2009.

[120] D.-H. Chae, T. Utikal, S. Weisenburger, H. Giessen, K. v. Klitzing, M. Lippitz, and J. Smet. Excitonic Fano Resonance in Free-Standing Graphene. *Nano Lett.*, 11:1379–1382, 2011.

[121] K. F. Mak, J. Shan, and T. F. Heinz. Seeing Many-Body Effects in Single- and Few-Layer Graphene: Observation of Two-Dimensional Saddle-Point Excitons. *Phys. Rev. Lett.*, 106:046401, 2011.

[122] K. F. Mak, M. Y. Sfeir, Y. Wu, C. H. Lui, J. A. Misewich, and T. F. Heinz. Measurement of the Optical Conductivity of Graphene.

*Phys. Rev. Lett.*, 101:196405, 2008.

[123] M. O. Scully. *Quantum Optics*. Cambridge University Press, 1997.

[124] M. Sprinkle, D. Siegel, Y. Hu, J. Hicks, A. Tejeda, A. Taleb-Ibrahimi, P. Le Fèvre, F. Bertran, S. Vizzini, H. Enriquez, S. Chiang, P. Soukiassian, C. Berger, W. A. de Heer, A. Lanzara, and E. H. Conrad. First Direct Observation of a Nearly Ideal Graphene Band Structure. *Phys. Rev. Lett.*, 103:226803, Nov 2009.

[125] D. Sun, C. Divin, C. Berger, W. A. de Heer, P. N. First, and T. B. Norris. Spectroscopic Measurement of Interlayer Screening in Multilayer Epitaxial Graphene. *Phys. Rev. Lett.*, 104:136802, Apr 2010.

[126] F. Wendler, H. Funk, M. Mittendorff, S. Winnerl, M. Helm, A. Knorr, and E. Malic. Efficient Auger scattering in Landau-quantized graphene. *Proc. SPIE*, 9361:936105–936105–7, 2015.

[127] W.-P. Li, J.-W. Yin, Y.-F. Yu, and Z.-W. Wang. Two-phonon relaxation processes of the graphene in the magnetic field. *Solid State Commun.*, 163:19 – 22, 2013.

[128] S. Fratini and F. Guinea. Substrate-limited electron dynamics in graphene. *Phys. Rev. B*, 77:195415, May 2008.

[129] T. Low, V. Perebeinos, R. Kim, M. Freitag, and P. Avouris. Cooling of photoexcited carriers in graphene by internal and substrate phonons. *Phys. Rev. B*, 86:045413, Jul 2012.

[130] F. Guinea, M. I. Katsnelson, and A. K. Geim. Energy gaps and a zero-field quantum Hall effect in graphene by strain engineering. *Nat. Phys.*, 6(1):30–33, 2010.

[131] N. Levy, S. A. Burke, K. L. Meaker, M. Panlasigui, A. Zettl, F. Guinea, A. H. Castro Neto, and M. F. Crommie. Strain-Induced Pseudo-Magnetic Fields Greater Than 300 Tesla in Graphene Nanobubbles. *Science*, 329(5991):544–547, 2010.

[132] R. D. Schaller and V. I. Klimov. High Efficiency Carrier Multiplication in PbSe Nanocrystals: Implications for Solar Energy Conversion. *Phys. Rev. Lett.*, 92:186601, 2004.

[133] R. D. Schaller, V. M. Agranovich, and V. I. Klimov. High-efficiency carrier multiplication through direct photogeneration of multi-excitons via virtual single-exciton states. *Nature Phys.*, 1:189–194, 2005.

[134] R. J. Ellingson, M. C. Beard, J. C. Johnson, P. Yu, O. I. Micic, A. J. Nozik, A. Shabaev, and A. L. Efros. Highly Efficient Multiple Exciton Generation in Colloidal PbSe and PbS Quantum Dots. *Nano Lett.*, 5(5):865–871, 2005. PMID: 15884885.

[135] I. Gur, N. A. Fromer, M. L. Geier, and A. P. Alivisatos. Air-Stable All-Inorganic Nanocrystal Solar Cells Processed from Solution. *Science*, 310(5747):462–465, 2005.

[136] G. D. Scholes and G. Rumbles. Excitons in nanoscale systems. *Nat. Mater.*, 5(9):683–696, September 2006.

[137] R. D. Schaller, M. Sykora, J. M. Pietryga, and V. I. Klimov. Seven Excitons at a Cost of One: Redefining the Limits for Conversion Efficiency of Photons into Charge Carriers. *Nano Lett.*, 6:424–429, 2006.

[138] G. Nair, L.-Y. Chang, S. M. Geyer, and M. G. Bawendi. Perspective on the Prospects of a Carrier Multiplication Nanocrystal Solar Cell. *Nano Lett.*, 11:2145–2151, 2011.

[139] N. M. Gabor, Z. Zhong, K. Bosnick, J. Park, and P. L. McEuen. Extremely Efficient Multiple Electron-Hole Pair Generation in Carbon Nanotube Photodiodes. *Science*, 325:1367–1371, 2009.

[140] R. Baer and E. Rabani. Can Impact Excitation Explain Efficient Carrier Multiplication in Carbon Nanotube Photodiodes? *Nano Lett.*, 10:3277–3282, 2010.

[141] S. Wang, M. Khafizov, X. Tu, M. Zheng, and T. D. Krauss. Multiple Exciton Generation in Single-Walled Carbon Nanotubes. *Nano Lett.*, 10:2381–2386, 2010.

[142] N. M. Gabor. Impact Excitation and Electron-Hole Multiplication in Graphene and Carbon Nanotubes. *Acc. Chem. Res.*, 46:1348–1357, 2013.

[143] Y. Kanemitsu. Multiple Exciton Generation and Recombination in Carbon Nanotubes and Nanocrystals. *Acc. Chem. Res.*, 46:1358–1366, 2013.

[144] P. T. Landsberg, H. Nussbaumer, and G. Willeke. Band-band impact ionization and solar cell efficiency. *J. Appl. Phys.*, 74:1451–1452, 1993.

[145] W. Shockley and H. J. Queisser. Detailed Balance Limit of Efficiency of p-n Junction Solar Cells. *J. Appl. Phys.*, 32:510–519, 1961.

[146] H. Aoki. Novel Landau level laser in the quantum Hall regime. *Appl. Phys. Lett.*, 48(9):559–560, 1986.

[147] T. Morimoto, Y. Hatsugai, and H. Aoki. Cyclotron radiation and emission in graphene - a possibility of Landau-level laser. *J. Phys. Conf. Ser.*, 150(2):022059, 2009.

[148] I. Gierz. Graphene optoelectronics: A fool's errand. *Nature Phys.*, 11:12–13, 2015.